2023

Tuning Microwave Losses in Superconducting Resonators

Alex Gurevich
Old Dominion University, agurevic@odu.edu

Original Publication Citation

Gurevich, A. (2023). Tuning microwave losses in superconducting resonators. *Superconductor Science and Technology*, *36*(6), 1-29, Article 063002. https://doi.org/10.1088/1361-6668/acc214

Superconductor Science and Technology

TOPICAL REVIEW • OPEN ACCESS

Tuning microwave losses in superconducting resonators

To cite this article: Alex Gurevich 2023 *Supercond. Sci. Technol.* **36** 063002

OPEN ACCESS
IOP Publishing
Superconductor Science and Technology
Supercond. Sci. Technol. **36** (2023) 063002 (29pp)
https://doi.org/10.1088/1361-6668/acc214

Topical Review

Tuning microwave losses in superconducting resonators

Alex Gurevich

Department of Physics and Center for Accelerator Science, Old Dominion University, 4600 Elkhorn Avenue, Norfolk, VA 23529, United States of America

E-mail: gurevich@odu.edu

Received 26 September 2022, revised 4 January 2023
Accepted for publication 7 March 2023
Published 28 April 2023

Abstract

The performance of superconducting resonators, particularly cavities for particle accelerators and micro cavities and thin film resonators for quantum computations and photon detectors, has been improved substantially by recent material treatments and technological advances. As a result, the niobium cavities have reached the quality factors $Q \sim 10^{11}$ at 1–2 GHz and 1.5 K and the breakdown radio-frequency (rf) fields H close to the dc superheating field of the Meissner state. These advances raise the questions of whether the state-of-the-art cavities are close to the fundamental limits, what these limits actually are, and to what extent the Q and H limits can be pushed by the materials nano structuring and impurity management. These issues are also relevant for many applications using high-Q thin film resonators, including single-photon detectors and quantum circuits. This topical review outlines basic physical mechanisms of the rf nonlinear surface impedance controlled by quasiparticles, dielectric losses and trapped vortices, as well as the dynamic field limit of the Meissner state. Sections cover methods of engineering an optimum quasiparticle density of states and superfluid density to reduce rf losses and kinetic inductance by pairbreaking mechanisms related to magnetic impurities, rf currents, and proximity-coupled metallic layers at the surface. A section focuses on mechanisms of residual surface resistance, which dominates rf losses at ultra low temperatures. Microwave losses of trapped vortices and their reduction by optimizing the concentration of impurities and pinning potential are also discussed.

Keywords: tunings, microwave, superconducting, resonators, quality factor

(Some figures may appear in colour only in the online journal)

1. Introduction

Low-dissipative superconducting resonators are instrumental in many applications, particularly quantum computations [1], single photon detectors [2–5], quantum memories [6] and cavities for particle accelerators [7–9]. They employ fully gapped s-wave superconductors with extremely low electromagnetic losses at temperatures $T \ll T_c$ and microwave or radio frequencies (rfs) $\hbar\omega \ll \Delta$, where $\Delta = 1.76 k_B T_c$ is the superconducting gap and T_c is the critical temperature [10–14]. The losses can be further reduced by encapsulating Josephson junctions in resonant cavities to eliminate radiation losses characteristic of thin film structures [5]. RF losses are quantified by the quality factor Q proportional to the ratio of

electromagnetic energy in the cavity to the power dissipated in the cavity wall [15]:

$$Q = \frac{\omega\mu_0 \int_V |\mathbf{H}(\mathbf{r})|^2 dV}{\oint_A R_s |\mathbf{H}(\mathbf{r})|^2 dA}, \quad (1)$$

where $\mathbf{H}(\mathbf{r},\omega)e^{-i\omega t}$ is the magnetic field in the cavity mode with the circular eigenfrequency $\omega = 2\pi\nu$ and R_s is the surface resistance. Generally, $R_s[H(\mathbf{r}),\mathbf{r}]$ varies along the surface due to trapped vortices, materials and topographic defects and the dependence of R_s on the rf field amplitude $H_a(\mathbf{r})$ for a particular resonant mode. Since $\omega \sim c/L$ is inversely proportional to the cavity size L, it is convenient to present equation (1) in the form $Q(B_a) = Z_0/\langle R_s\rangle$, where $B_a = \mu_0 H_a$, $Z_0 = c\mu_0\alpha$, c is the speed of light, $\langle\ldots\rangle$ means averaging of R_s over the cavity surface, and $\alpha \sim 1$ is a geometrical factor [7]. The scale of Z_0 is set by the vacuum impedance $\mu_0 c = 377\,\Omega$.

The best Nb cavities can achieve extremely high quality factors $Q \sim 10^{10}$–10^{11} corresponding to $R_s \sim 5$ nΩ and sustain accelerating fields up to 50 MV m^{-1} at $T = 1.5$–2 K and $\nu = 1.3$–2 GHz [16, 17]. The peak fields $B_a \simeq 200$ mT at the equatorial surface of these cavities approach the thermodynamic critical field $B_c \approx 200$ mT of Nb at 2 K [7–9]. At $B_a \simeq B_c$ the screening rf current density flowing at the inner cavity surface is close to the depairing current density $J_c \simeq B_c/\mu_0\lambda$—the maximum dc current density a superconductor can carry in the Meissner state [18–21], where λ is the London penetration depth. Thus, the breakdown fields of the best Nb cavities have nearly reached the dc superheating field $B_s \simeq B_c$ [22–27]. The Q factors can be increased by material treatments, such as high temperature (600 °C–800 °C) annealing followed by low temperature (100 °C–120 °C) baking which not only increase $Q(B_a)$ and the breakdown field but also reduce deterioration of Q at high fields [28–32]. High temperature treatments combined with the infusion of nitrogen, titanium or oxygen can produce an anomalous increase of $Q(B_a)$ with B_a [33–41] and $Q \simeq (3$–$4) \times 10^{11}$ at 1.5 K and $\simeq 5 \times 10^{10}$ at 2 K and 1.3 GHz [32]. These advances raise questions about the fundamental limits of rf losses and the breakdown fields in high-Q resonators and the extent to which these limits can be pushed by surface nano-structuring and impurity management. In high-power rf applications, superconductors with high T_c and B_c (for example, Nb_3Sn) can only be used in the form of thin film [42] or multilayer [43, 44] coatings of Nb cavities. Thin film superconducting resonators have been widely used in single-photon detectors, quantum memory and quantum computations [1–6].

The fact that microwave losses can be optimized by impurity management can be understood from the BCS theory, according to which a superconductor with no impurities and an ideal surface does not have the lowest surface resistance [10, 11]. For instance, R_s of a type-II superconductor with a large Ginzburg–Landau (GL) parameter $\kappa = \lambda/\xi \gg 1$ at $T \ll T_c$ and $\hbar\omega \ll k_B T$ has the form [44]

$$R_s = \frac{\mu_0^2\omega^2\lambda^3\Delta}{\rho_s k_B T} \ln\left[\frac{C_1 k_B T}{\hbar\omega}\right] \exp\left[-\frac{\Delta}{k_B T}\right] + R_i. \quad (2)$$

The first term in the rhs of equation (2) is the BCS surface resistance $R_{BCS}(T)$ caused by absorption of low-energy ($\hbar\omega \ll k_B T$) microwave photons by a small density of quasiparticles resulting from thermal dissociation of Cooper pairs [5, 10, 11, 44]. Here Δ is a superconducting gap, $\rho_s = 1/\sigma_s$ is the resistivity in the normal state, ξ is the coherence length, $C_1 \approx 9/4$ and k_B and $\hbar$ are the Boltzmann and Planck constants, respectively. The residual surface resistance R_i in equation (2) which remains finite or decreases much slower than $\exp(-\Delta/k_B T)$ at $T \to 0$ has been observed in many superconductors [13, 14] but it is not accounted for in the BCS model.

As follows from equation (2), R_{BCS} can be tuned by the materials disorder. For a spherical Fermi surface, Δ is independent of the mean free path on nonmagnetic impurities l_i [18], so the dependence of R_{BCS} on l_i is determined by the factor λ^3/ρ_s. Here $\rho_s = p_F/n_0 e^2 l_i$ and $\lambda \simeq \lambda_0(1+\xi_0/l_i)^{1/2}$ [18], where $\lambda_0 = (m/n_0 e^2\mu_0)^{1/2}$ and $\xi_0 = \hbar v_F/\pi\Delta$ are the London penetration depth and the coherence length in a clean material at $T = 0$, respectively, p_F is the Fermi momentum, n_0 is the carrier density, and e is the electron charge. Hence, $\lambda^3/\rho_s \propto l_i(1+\xi_0/l_i)^{3/2}$ is minimum at $l_i = 0.5\xi_0$, which translates to the optimum $l_i \approx 20$ nm for Nb. Microscopic calculations [12] have shown that $R_{BCS}(l)$ does have a minimum at $l_i \sim \xi_0$ and remains finite in the clean limit $l_i \gg \xi_0$ analogous to the anomalous skin effect in metals [10]. It turns out that R_s can be further reduced by surface nanostructuring and magnetic impurities [45, 46].

The surface resistance is determined by multiple competing mechanisms so the material treatments which reduce R_s in a certain region of T, ω and H can in turn increase R_s outside that region. For instance, equation (2) suggests that s-wave superconductors with no nodes in the quasiparticle gap and the highest T_c would have the lowest $R_{BCS}(T)$ at $T \ll T_c$. Yet the accelerating cavities are built of Nb with its modest $T_c = 9.2$ K as compared to $T_c = 18.2$ K of Nb_3Sn or $T_c \approx 40$ K of MgB_2 or T_c up to 55 K of iron pnictides [47]. This is because materials with T_c higher than $T_c^{Nb} = 9.2$ K are type-II superconductors with the lower critical field B_{c1} smaller than $B_{c1} \simeq 170$–180 mT of Nb which has the highest B_{c1} among all superconductors [47–49]. This makes Nb best protected against penetration of vortices which can greatly increase R_s at $B_a > B_{c1}$. Alloying a superconductor with impurities to reduce R_s at the optimum $l_i \simeq \xi_0/2$ changes $\lambda \simeq \lambda_0(1+\xi_0/l_i)^{1/2} \to \sqrt{3}\lambda_0$ and $\xi \simeq \sqrt{l_i\xi_0} \to \xi_0/\sqrt{2}$, which decreases $B_{c1} = (\phi_0/4\pi\lambda^2)[\ln(\lambda/\xi) + 1/2]$ by more than 50% and reduces the superheating field B_s at which the Meissner state becomes unstable [22–27]. This illustrates how a lower R_s at weak fields is achieved at the expense of larger R_s at strong fields.

Reducing microwave losses in the vortex-free Meissner state requires optimization of the quasiparticle R_s, while widening the field region of the Miessner state. This could

be achieved by thin film or multilayer coating Nb resonators with high-T_c but low B_{c1} superconductors [43]. Here, the properties of such materials in the normal state become important. For instance, Nb_3Sn has high T_c and low R_s in weak rf fields [50–52], but its thermal conductivity is some 3 orders of magnitude lower than that of clean Nb at 2 K [53]. Thus, despite its better performance at low fields, Nb_3Sn is more prone to penetration of vortices and rf overheating which degrades $Q(B_a)$ at higher fields (even a few micron thick Nb_3Sn film on the inner surface of the Nb cavity can double the thermal impedance of the cavity wall [9]). Another source of rf losses comes from second phase precipitates and weakly coupled grain boundaries in polycrystalline superconductors with short coherence lengths, such as Nb_3Sn [54–56] and iron pnictides [57].

At very low temperatures the residual resistance R_i becomes the dominant source of dissipation. This can result from subgap states at the quasiparticle energies $|\epsilon| < \Delta$ revealed by tunneling measurements [58, 59]. The subgap states have been attributed to multiple mechanisms, but none of them has been unambiguously established as a prime source of R_i. Besides the subgap states, R_i has also been attributed to two-level states (TLSs) in surface oxides [5, 60, 61], grain boundaries [54–57] and non-superconducting second phase precipitates [7, 8]. A significant contribution to R_i can come from trapped vortices [62–70] which appear during the cooldown of a superconductor through T_c in stray magnetic fields. This is also essential for thin films in quantum circuits [1, 71–73] in which vortices can be generated by very weak perpendicular stray fields as B_{c1} is greatly reduced by demagnetizing effects [74, 75]. Spontaneous vortex-antivortex pairs and vortex loops can appear upon cooling with a finite temperature ramp rate [76, 77] or be produced by thermal fluctuations [78]. Because of the extremely small $R_{\rm BCS}(T)$ the losses in high-Q resonators can be dominated by a small number of trapped vortices oscillating under rf field. Trapped vortices can bundle together, forming hotspots which have been revealed both in Nb cavities [28, 79, 80] and thin film structures [81, 82]. Reducing R_i at low rf fields involves effective pinning of trapped vortices without degradation of quasiparticle and TLS surface resistance [71–73].

This paper gives an overview of basic physical mechanisms which can control both the quasiparticle and residual surface resistance, including subgap states, TLS, nonlinear current pairbreaking, trapped vortices and a dynamic superheating field which determines the field limit of a nonequilibrium Meissner state. Reducing R_s by engineering an optimum quasiparticle density of states (DOSs) using pairbreaking mechanisms, such as magnetic impurities, rf currents and proximity-coupled metallic overlayers are discussed. Furthermore, mitigation of microwave losses by surface nanostructuring, impurity management and optimization of pinning of trapped vortices are considered. This review primarily focuses on superconducting parameters which can be tuned to enhance the performance of high-Q resonators while not addressing specific atomic mechanisms by which these parameters are affected by material treatments.

2. Complex conductivity of superconductors

The electromagnetic response of a superconductor in a weak field is described by the following relation for the Fourier components of the current density $\mathbf{J}(\mathbf{k},\omega)$ induced by the magnetic vector potential $\mathbf{A}(\mathbf{k},\omega)$ (in the gauge div$\mathbf{A} = 0$) [10, 18]

$$\mathbf{J}(\mathbf{k},\omega) = -K(\mathbf{k},\omega)\mathbf{A}(\mathbf{k},\omega), \tag{3}$$

where $\mathbf{B} = \nabla \times \mathbf{A}$, and the complex electromagnetic kernel $K(k,\omega)$ depends on the circular frequency $\omega = 2\pi\nu$ and the wave vector $\mathbf{k}$ of the rf field. The real part of K describes the Meissner effect caused by the superconducting condensate, so that $K(0,0) = 1/\mu_0\lambda^2$ in the static local limit. The imaginary part of K describes dissipative processes caused by quasiparticles driven by the rf field. The BCS theory gives general formulas for $K(k,\omega,T,l_i)$ which also depends on the mean free path l_i due to scattering of electrons on impurities [10, 83]. Although the BCS model captures the fundamentals of electrodynamics of superconductors, it can hardly be used for quantitative calculations of $K(k,\omega,T,l_i)$ for Nb or Pb or Nb_3Sn in which the electron–phonon coupling is not weak [84]. Superconductors with strong electron–phonon interaction are described by the Eliashberg theory [84] in which $K(k,\omega,T,l_i)$ was obtained in [11]. Microwave conductivity of different superconductors described by the Eliashberg theory was calculated in [85–88].

The power P dissipated per unit surface area of a superconductor is determined by the real part of the surface impedance $Z(\omega) = R_s + iX$:

$$P = \frac{R_s}{2}H_a^2, \tag{4}$$

where H_a is the amplitude of the rf field $H(t) = H_a\cos\omega t$ at the surface. The surface resistance R_s can be expressed in terms of $K(k,\omega,T,l_i)$ by integral relations [10–12, 88] which depend on the way the electrons are scattered by the surface (specular or diffusive). Using these results, $Z(\omega,T)$ can be calculated numerically for arbitrary T, ω and l_i for a particular material like Nb [86, 87]. The situation simplifies at low temperatures $k_{\rm B}T \ll \Delta$ and frequencies much lower than the gap frequency $\nu \ll \nu_{\rm g} = \Delta/\pi\hbar$ at which high-Q resonators operate. For instance, $\nu_{\rm g}({\rm GHz}) = 74T_c$ (K)$= 680$ GHz for Nb is much larger than the rf frequency domain 0.1–5 GHz in which the absorption of single photons cannot break the Cooper pairs. In this case, the superconducting condensate follows nearly instantaneously to the driving rf field, while the dissipative current of thermally-activated quasiparticles can have much longer relaxation times determined by inelastic scattering on phonons [83].

In the most transparent case of $\lambda \gg \xi$, the rf magnetic and electric fields are confined in the layer of thickness $\simeq\lambda$ at the surface, where λ is the static London penetration depth. Dissipation comes from a small 'normal' component of the current density J_n oscillating in-phase with the driving electric field. Both in-phase and out-of phase components of $\mathbf{J}(\mathbf{r},t)$ can be calculated from the Maxwell equations combined with

equation (3), which generally gives a nonlocal integral relation between $\mathbf{J}(\mathbf{r},\omega)$ and $\mathbf{A}(\mathbf{r},\omega)$ in the coordinate space [10]. In the limit of $\lambda \gg \xi$, the relation between $\mathbf{J}(\mathbf{r},\omega)$ and $\mathbf{A}(\mathbf{r},\omega)$ simplifies to the local 'ohmic' form with a frequency-dependent complex conductivity $\sigma(\omega) = \sigma_1(\omega) - i\sigma_2(\omega)$:

$$\mathbf{J}(\mathbf{r}\omega) = (\sigma_1 - i\sigma_2)\mathbf{E}(\mathbf{r},\omega). \tag{5}$$

The reactive part σ_2 responsible for the Meissner effect is given by

$$\sigma_2 = 1/\omega\mu_0\lambda^2. \tag{6}$$

The surface impedance is calculated using the standard formula of the electromagnetic theory [15] in the limit of weak Ohmic dissipation, $\sigma_1 \ll \sigma_2$:

$$Z = \left[\frac{i\mu_0\omega}{\sigma_1 - i\sigma_2}\right]^{1/2} \simeq \frac{\mu_0\omega\sigma_1}{2\sigma_2^2}\sqrt{\frac{\sigma_2}{\mu_0\omega}} + i\sqrt{\frac{\mu_0\omega}{\sigma_2}}. \tag{7}$$

Substituting here equation (6) yields

$$2R_s = \mu_0^2\omega^2\lambda^3\sigma_1(\omega), \qquad X_s = \mu_0\omega\lambda. \tag{8}$$

The dissipative conductivity $\sigma_1(\omega)$ evaluated from the Mattis–Bardeen theory [10, 11] at $\hbar\omega \ll \Delta$, $T \ll T_c$ and $l_i < \xi_0$ takes the form [5, 44]:

$$\sigma_1 = \frac{4\sigma_n\Delta}{\hbar\omega}\sinh\left[\frac{\hbar\omega}{2k_BT}\right]K_0\left[\frac{\hbar\omega}{2k_BT}\right]e^{-\Delta/k_BT}, \tag{9}$$

where $K_0(x)$ is a modified Bessel function. At $\nu = 1-2$ GHz and $T = 1-2$ K, we have $\hbar\omega/2k_BT \sim 10^{-2}$ so equation (9) can be expanded in $\hbar\omega/2k_BT \ll 1$ using $K_0(x) \simeq \ln(2/x) - \gamma_E$ at $x \ll 1$, where $\gamma_E = 0.577$ is the Euler constant. Hence, $\sigma_1 \simeq (2\sigma_n\Delta/k_BT)\ln(C_1k_BT/\hbar\omega)e^{-\Delta/k_BT}$, where $C_1 = 4e^{-\gamma_E} \approx 9/4$. This σ_1 combined with equation (8) yield the BCS surface resistance in equation (2).

In type-I superconductors such as Al, Sn, Ta or Pb the electromagnetic response becomes nonlocal and the screening current density does not decay exponentially over the London penetration depth λ. In the extreme Pippard limit $\xi_0 \gg \lambda$, the effective field penetration depth $\tilde{\lambda} \simeq 0.65(\lambda^2\xi_0)^{1/3}$ can exceed λ [18]. For instance, in clean Al with $\xi_0 = 1500$ nm and $\lambda = 16$ nm we get $\tilde{\lambda} \approx 47$ nm, whereas Sn with $\xi_0 = 230$ nm and $\lambda = 34$ nm has $\tilde{\lambda} \approx 42$ nm. Calculations of the surface impedance of Al and Sn films using the full Mattis–Bardeen electromagnetic kernel $K(\mathbf{k},\omega)$ [10] has shown that the nonlocality makes R_s dependent on the film thickness d up to $d \sim \xi_0$ [89].

2.1. Subgap states

In the BCS model, the quasiparticle DOSs $N(\epsilon)$ vanishes at energies $|\epsilon| < \Delta$, even if weak scattering on nonmagnetic impurities present [18, 83, 90]. It is the feature of $N(\epsilon)$ which ensures the exponentially small $R_{\rm BCS}(T)$ and $R_i = 0$ in equation (2). Yet, many tunneling measurements of $N(\epsilon)$ [58, 59] have shown that $N(\epsilon)$ differs from the idealized DOS which diverges at $\epsilon = \Delta$ and vanishes at $\epsilon < \Delta$, as shown in figure 1. In the observed $N(\epsilon)$ the gap singularities at $\epsilon = \Delta$ are smeared out and subgap states with a finite $N(\epsilon)$ appear at $\epsilon < \Delta$. Such DOS has often been described by the phenomenological Dynes model [58] in which

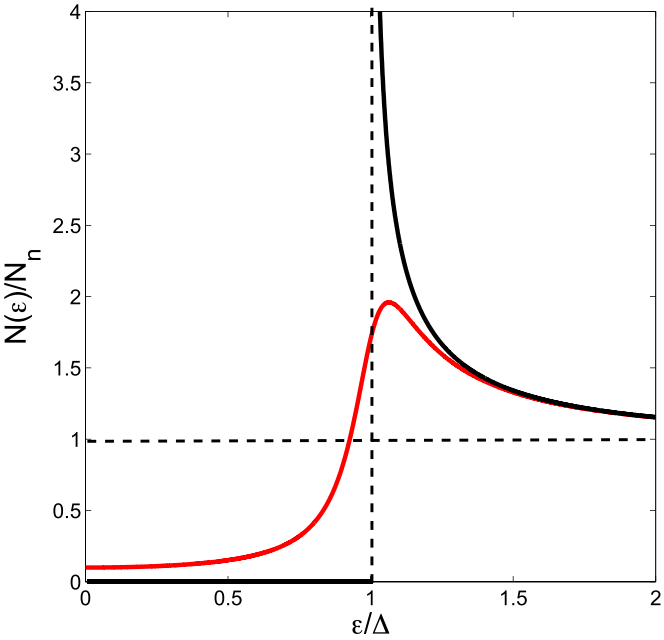

Figure 1. $N(\epsilon)$ in the BCS model (black) and $N(\epsilon)$ described by equation (10) for $\Gamma/\Delta = 0.2$ (red).

$$N(\epsilon) = \mathrm{Re}\frac{N_n(\epsilon - i\Gamma)}{\sqrt{(\epsilon - i\Gamma)^2 - \Delta^2}}. \tag{10}$$

Here the damping parameter Γ quantifies a finite lifetime of quasiparticles $\sim\hbar/\Gamma$, resulting in a finite DOS $N(0) \simeq \Gamma N_n/\Delta$ at the Fermi level. Tunneling conductance measurements on Nb [91, 92] and Nb_3Sn [93] have indeed revealed a finite $N(\epsilon)$ at $\epsilon < \Delta$ (a review of tunneling measurements of $N(\epsilon)$ and applications of equation (10) are given in [59]). The physics of subgap states is not fully understood (see e.g. reviews [59, 94] and the references therein). Many mechanisms of subgap states have been suggested in the literature, including inelastic scattering of quasiparticles on phonons [95], Coulomb correlations [96], anisotropy of the Fermi surface [97], inhomogeneities of the BCS pairing constant [98], magnetic impurities [90], spatial correlations in impurity scattering [90, 99], diffusive surface scattering [100] or quasiparticles trapped by inhomogeneities of $\Delta(\mathbf{r})$ [101]. The phenomenological equation (10) captures the observed broadening of the DOS peaks at $\epsilon \approx \Delta$ but it can hardly describe the low-energy tails in $N(\epsilon)$ due to, for example, energy-dependent electron–phonon relaxation times [102]. Details of exponential or power-law energy tails in $N(\epsilon)$ at $|\epsilon| \ll \Delta$ can be essential for the behavior of $R_i(T)$ at ultra low temperatures [101]. Yet, the widely used equation (10) in which all microscopic mechanisms are included in a single parameter Γ is rather useful to address qualitative effects of the DOS broadening on R_s.

The broadening of the DOS gap peaks reduces T_c and Δ in a way similar to the pairbreaking effect of magnetic impurities

[90]. For instance, T_c decreases with Γ and vanishes at $\Gamma_c = \Delta_0/2$, where Δ_0 is the gap at $T = 0$ and $\Gamma = 0$ [45, 103]. For weak DOS broadening $\Gamma \ll k_B T_{c0}$, we have [45, 103]

$$T_c = T_{c0} - \frac{\pi\Gamma}{4}, \tag{11}$$

$$\Delta \simeq \Delta_0 - \Gamma - \frac{\pi^2 \Gamma T^2}{6\Delta_0^2}, \quad T \ll T_c. \tag{12}$$

A finite DOS at $\varepsilon = 0$ in the Dynes model yields a quadratic temperature dependence of $\Delta(T)$ instead of the BCS behavior of $\Delta(T) \simeq \Delta_0 - \sqrt{2\pi k_B T \Delta_0}\exp(-\Delta_0/k_B T)$ at $T \ll T_c$ [83]. The DOS broadening increases the magnetic penetration depth λ at $T \ll T_c$ in the dirty limit as following [45, 103]:

$$\frac{1}{\lambda^2} = \frac{2\mu_0\Delta}{\hbar\rho_n}\tan^{-1}\frac{\Delta}{\Gamma}, \tag{13}$$

This reproduces the BCS result $\lambda^2 = \hbar\rho_n/\pi\mu_0\Delta$ at $T = \Gamma = 0$ [83]. The dependence of λ on the mean free path l_i at $T = \Gamma = 0$ is given by [11]:

$$\frac{1}{\lambda^2} = \frac{1}{a\lambda_0^2}\left[\frac{\pi}{2} - \frac{\cos^{-1}(a)}{\sqrt{1-a^2}}\right], \quad a < 1 \tag{14}$$

$$\frac{1}{\lambda^2} = \frac{1}{a\lambda_0^2}\left[\frac{\pi}{2} - \frac{\cosh^{-1}(a)}{\sqrt{a^2-1}}\right], \quad a > 1 \tag{15}$$

where $\lambda_0 = (m/\mu_0 n_0 e^2)^{1/2}$ and the parameter $a = \pi\xi_0/2l_i$ quantifies scattering on impurities, so that $a \ll 1$ and $a \gg 1$ correspond to the clean and the dirty limits, respectively. As l_i decreases, $\lambda(l_i)$ increases from λ_0 in the clean limit $l_i \gg \xi_0$ to $\lambda \simeq \lambda_0(\xi_0/l_i)^{1/2}$ in the dirty limit, $l_i < \xi$. In turn, the coherence length $\xi(l_i)$ decreases from ξ_0 at $l_i \gg \xi_0$ to $\xi \simeq \sqrt{l_i\xi_0}$ if $l_i \ll \xi_0$ [18]. In the BCS model, weak scattering of electrons on nonmagnetic impurities does not affect $\Delta(T)$, T_c and $B_c(T)$ of a superconductor with a spherical Fermi surface [18, 90]. This is no longer the case for strong impurity scattering and anisotropic Fermi surface [90]. Strong electron–phonon coupling gives rise to a power-law temperature dependence of $\lambda(T)$ at $T \ll T_c$ due to the contribution of low-energy phonons [104].

2.2. Residual surface resistance

The observed temperature dependence of $R_s(T)$ on s-wave superconductors follows equation (2) with $\Delta = c_1 k_B T_c$, where c_1 is slightly higher than the BCS prediction $c_1 = 1.76$ due to the effects of strong electron–phonon coupling [84]. Many extrinsic mechanisms of the residual surface resistance have been pointed out in the literature, including lossy oxides or metallic hydrides in Nb [7, 8], trapped vortices [62–70], grain boundaries [105–107], or TLSs [5, 108, 109]. The effect of metallic hydrides has been well documented for Nb cavities [110, 111] and films [112–114]. Formation of metallic hydride precipitates from over-saturated solid solutions of H interstitials is characteristic of Nb [115]. In films, R_i can be increased by the surface roughness and absorption of noble gases [112–114]. These intrinsic factors can be mitigated by high temperature (600 °C–800 °C) annealing [8] of by pushing trapped vortices out by temperature gradients [64, 80, 116, 117].

A residual resistance produced by the subgap states can be obtained by incorporating the Dynes DOS into the BCS expression for $R_s(T)$ [44, 45]:

$$R_s = R_1 \sinh\left(\frac{\hbar\omega}{2k_B T}\right)\int_{-\infty}^{\infty}\frac{[n(\hbar\omega+\epsilon)n(\epsilon) + m(\hbar\omega+\epsilon)m(\epsilon)]\mathrm{d}\epsilon}{\cosh(\epsilon/2k_B T)\cosh[(\epsilon+\hbar\omega)/2k_B T]}, \tag{16}$$

$$n(\epsilon) = \mathrm{Re}\frac{(\epsilon - i\Gamma)}{\sqrt{(\epsilon-i\Gamma)^2 - \Delta^2}}, \qquad m(\epsilon) = \mathrm{Re}\frac{\Delta}{\sqrt{(\epsilon-i\Gamma)^2-\Delta^2}}, \tag{17}$$

where $R_1 = \mu_0^2\omega\lambda^3/4\hbar\rho_s$ and $n(\epsilon)$ and $m(\epsilon)$ are real parts of retarded normal and anomalous quasiclassical Green's functions [83]. Equation (16) with $\Gamma = 0$ reproduces $R_{BCS}(T)$ in equation (2). Complex conductivity in the Dynes model and arbitrary mean free path was calculated in [103]. In addition to the BCS part $R_{BCS} \propto \exp(-\Delta/k_B T)$, equation (16) accounts for a residual $R_i(T)$ that is not exponentially small at $T \ll T_c$ [45]:

$$R_i(T) = \frac{\mu_0^2\omega^2\lambda^3\Gamma^2}{2\rho_n(\Delta^2+\Gamma^2)}\left[1 + \frac{4\pi^2 k_B^2 T^2\Delta^2}{3(\Delta^2+\Gamma^2)^2}\right], \quad k_B T < \Gamma \tag{18}$$

where $\Delta(\Gamma)$ is given by equation (12). According to equation (18), getting $R_i \simeq 4$ nΩ at 1.5 GHz for Nb with $\lambda = 40$ nm and $\rho_s = 1$ nΩ·m requires $\Gamma \simeq 0.03\Delta$. The finite R_i at $T = 0$ results from the Dynes model assumption that Γ is independent of ε and T. In the case of a power law $N_s(\epsilon)$ at $\epsilon \ll \Delta$ (see, e.g. [94, 101]), one could expect a power law $R_s \propto T^n$ at ultralow temperatures. Shown in figure 2 is the Arrhenius plot of $R_s(T)$ calculated from equations (16) and (17) for different ratios of Γ/Δ_0. At higher temperatures $\ln R_s(T)$ follows the BCS linear dependence on $\Delta/k_B T$ and levels off as T decreases. The latter is indicative of a residual resistance resulting from the broadening of the DOS gap peaks. One can see that at low temperatures $R_s(T,\Gamma)$ increases as Γ increases but at higher T this trend reverses and $R_s(T,\Gamma)$ decreases as Γ increases.

The non-monotonic dependence of R_s on Γ, shown in figure 2, can be understood by noticing that R_i in equation (18) increases with Γ. In turn, the reduction R_s with Γ at higher T comes from the reduction of the logarithmic factor in equation (2). In the BCS model with $\Gamma = 0$ the factor $\ln(C_1 k_B T/\hbar\omega)$ in R_{BCS} occurs because the square root singularities in the DOS at $\epsilon = \Delta$ and $\epsilon = \Delta \pm \hbar\omega$ merge at $\omega \to 0$ and produce a pole in the integrand of equation (16). However, if $\Gamma > 0$, the gap singularities in $n(\epsilon)$ and $m(\epsilon)$ broaden into peaks of width $\sim\Gamma$ cutting off the divergence in equation (16) at $\omega = 0$. At $\Gamma > \hbar\omega$ but $\Gamma \ll k_B T$ integration of these peaks in equation (16) at $\epsilon \simeq \Delta$ yields a logarithmic term similar to that in equation (2) but with the energy cutoff Γ instead of $\hbar\omega$.

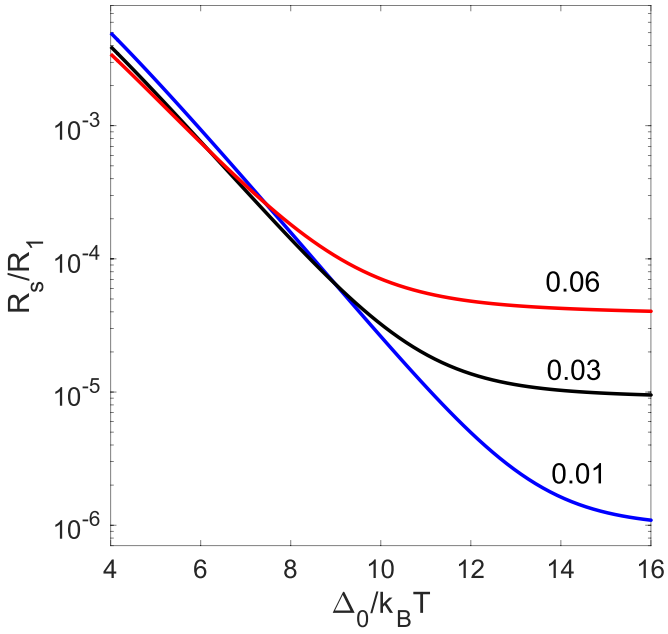

Figure 2. Arrhenius plot for $R_s(T)$ calculated from equation (16) for Nb with $\Delta = 17.5$ K at 1.5 GHz and different ratios of Γ/Δ. Reprinted figure with permission from [45], Copyright (2019) by the American Physical Society.

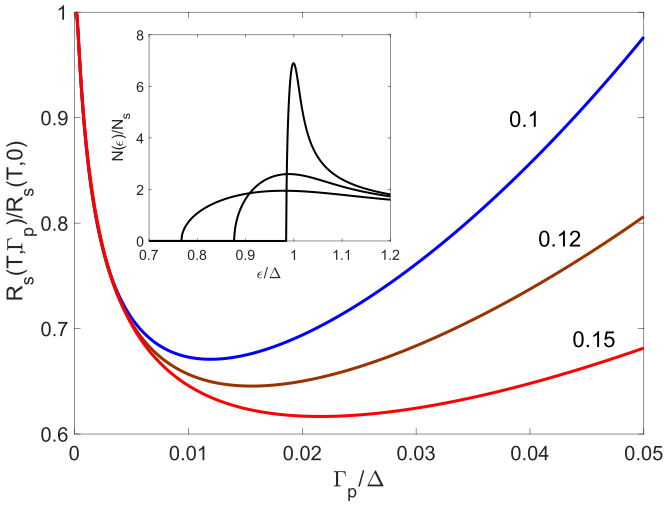

Figure 3. Minimum in the surface resistance $R_s(\Gamma_p)$ as a function of the spin-flip pairbreaking parameter Γ_p calculated from equations (16) and (22) at $\hbar\omega = 0.005\Delta$ and $k_BT/\Delta = 0.1,$ 0.12, 0.15. Inset shows $N(\epsilon)$ calculated at $\Gamma_p/\Delta = 0.001,$ 0.02, 0.05. Reprinted figure with permission from [45], Copyright (2019) by the American Physical Society.

The smearing of the DOS gap peaks can be qualitatively taken into account by the following replacement in equation (2):

$$\ln\frac{k_BT}{\hbar\omega} \to \ln\frac{k_BT}{\Gamma}. \tag{19}$$

Hence, broadening the peaks in the DOS reduces $R_s(T)$ at temperatures at which R_i is negligible. At 2 K and 1 GHz we have $k_BT/\hbar\omega \sim 10^2$, so even weak broadening with $\Gamma = 0.02\Delta$ causes a two-fold reduction of R_s. Broadening the peaks in the DOS can be used to reduce the rf losses by pairbreaking mechanisms, as discussed below.

3. Reduction of R_s by pairbreaking mechanisms

In this section, we discuss the ways by which R_s can be reduced by tuning the DOS by pairbreaking mechanisms related to magnetic impurities, proximity-coupled metallic overlayers and rf current. The latter results in a microwave suppression of $R_s(B_a)$ and its non-monotonic dependence on the rf field amplitude.

3.1. Magnetic impurities

It is unclear how the Dynes parameter Γ could be tuned, but R_s can be reduced by magnetic impurities, the concentration of which can be varied by material treatments [45, 118, 119]. The spin-flip scattering on magnetic impurities reduces T_c, smears the gap singularities in the DOS and decreases the quasiparticle gap [21]:

$$\epsilon_g = \left(\tilde{\Delta}^{2/3} - \Gamma_p^{2/3}\right)^{3/2}. \tag{20}$$

Here $\Gamma_p = \hbar/2\tau_s$, where the spin-flip scattering time τ_s is inversely proportional to the volume density of magnetic impurities [21, 90]. If the Dynes broadening of the DOS is disregarded and only the effect of magnetic impurities is taken into account, the quasiparticle gap ϵ_g in equation (20) is smaller than the order parameter $\tilde{\Delta}$ [21]:

$$\tilde{\Delta} = \Delta_0 - \frac{\pi}{4}\Gamma_p, \qquad \Gamma_p \ll \Delta. \tag{21}$$

Here Δ_0 is the order parameter in the absence of magnetic impurities. The broadening of the DOS peaks increases with Γ_p as shown in the inset of figure 3.

The microwave conductivity and the factors $n(\epsilon) = \mathrm{Re}\cosh\theta$ and $m(\epsilon) = \mathrm{Re}\sinh\theta$ in equation (16) were calculated in [45, 118, 119] by solving the Usadel equation which takes into account the magnetic pairbreaking [83, 90]:

$$\epsilon\sinh\theta + i\Gamma_p\cosh\theta\sinh\theta = \tilde{\Delta}\cosh\theta. \tag{22}$$

The effect of magnetic impurities on R_s was calculated in [45]. The results are shown in figure 3, where $R_s(\Gamma_p)$ is plotted as a function of Γ_p at different temperatures. There is a minimum in $R_s(\Gamma_p)$ resulting from interplay of the DOS broadening which reduces R_s as Γ_p increases, and the reduction of the quasiparticle gap ϵ_g which increases R_s with Γ_p. The position of the minimum in $R_s(\Gamma_p)$ shifts to larger Γ_p as T increases. Thus, incorporation of a small density of magnetic impurities in a superconductor can noticeably (by $\sim$ 30%–40%) decrease the surface resistance at low temperatures. The conditions for the minimum in $R_s(\Gamma_p)$ can be evaluated using the Abrikosov–Gor'kov theory of weak magnetic scattering in which T_c vanishes at $\Gamma_p = \hbar/2\tau_s = \Delta_0/2$ [90]. The latter implies that magnetic impurities suppress superconductivity if the spin flip mean free path $l_s = v_F\tau_s$ becomes of the order

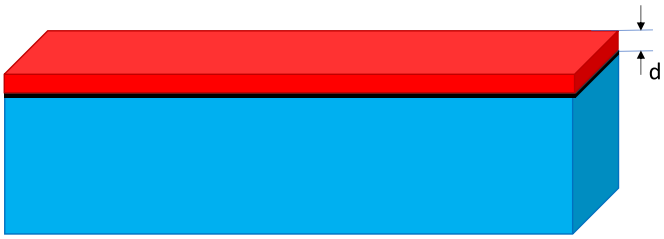

Figure 4. A metallic (N) layer of thickness d (red) coupled by the proximity effect to the bulk superconducting (S) substrate (blue). The black layer between N and S depicts a resistive interface barrier.

of the size of the Cooper pair, $\xi_0 = \hbar v_F/\pi\Delta_0$. The values of $\Gamma_p \simeq (0.01\text{–}0.02)\Delta$ in figure 3 correspond to $l_s \sim 10^2\xi_0$ if no bound quasiparticle states on magnetic impurities occur [90]. Magnetic impurities associated with oxygen vacancies in the native surface oxide of Nb have been revealed by tunneling measurements [91].

3.2. Proximity-coupled normal layer at the surface

Another tunable pairbreaking mechanism of reducing R_s involves a thin metallic (N) layer coupled to the bulk superconductor (S) by the proximity effect as shown in figure 4. Such an N layer models a generic surface oxide structure of superconducting materials, particularly a 1–2 nm thick metallic NbO suboxide sandwiched between the dielectric NbO_2—Nb_2O_5 oxides at the surface and the bulk Nb. This model was investigated in [45, 46] in which the Usadel equations were solved to calculate a position-dependent quasiparticle density of states $N_n(\epsilon, x)$ across a thin N layer coupled to the bulk superconductor, and their effect on the surface resistance. The DOS profile in the N layer can be inferred from scannong tunnely spectroscopy [120, 121].

The DOS profile and R_s are controlled by the parameters α and β which quantify the thickness of N layer and a resistive N–S interface barrier, respectively:

$$\alpha = \frac{dN_n}{\xi_s N_s}, \qquad \beta = \frac{4e^2}{\hbar} R_B N_n \Delta d. \tag{23}$$

Here d is the thickness of N layer, $\xi_s = (D_s/2\Delta)^{1/2}$ is the coherence length in the bulk superconductor with nonmagnetic impurities, D_s is the electron diffusivity proportional to the conductivity $\sigma_{n,s} = 2e^2 N_{n,s} D_{n,s}$ in the normal state, N_s and N_n are the respective DOS at the Fermi surface in the normal state, the subscripts n and s label the parameters of the N layer and the S substrate, respectively, and R_B is a contact resistance between N and S. The properties of the structure shown in figure 4 can be tuned by material treatments which change the thickness and conductivity of the N layer and the interface resistance R_B. For instance, $R_B(T)$ can either increase or decrease with T depending on the heat treatment which can change R_B by several orders of magnitude, as was shown for the YBCO-Ag interface [122, 123]. Complexities of the Schottky barrier between different materials are not fully understood [124], but the dependence of $R_s(T)$ on the interface resistance can be used to optimize R_s.

The thickness of the N layer and the interface resistance which control the strength of proximity coupling of the N layer with the S substrate, strongly affect the DOS profile at the surface. Shown in figure 5 are the DOS in the N layer much thinner than the proximity length $\xi_n = (\hbar D_n/2\Delta)^{1/2}$ and the DOS at the S side of the N–S interface calculated in [45] for different values of β at $\Gamma = 0$. For strong coupling $\beta \ll 1$, the DOS in the N layer has a sharp peak at $\epsilon \simeq \Delta$ and drops to zero below the minigap energy $\epsilon_0 < \Delta$ characteristic of N–S proximity-coupled structures [125, 126]. If $\beta \ll 1$ the proximity effect makes the N layer superconducting with $\epsilon_0 \approx \Delta$. As R_B increases, the minigap in the N layer decreases and the DOS approaches N_n for a decoupled N layer at $\beta \to \infty$. Here $\epsilon_0(\beta)$ at $\Gamma = 0$ is determined by the equation [45]:

$$\beta = \frac{\Delta}{\epsilon_0}\left(\frac{\Delta - \epsilon_0}{\Delta + \epsilon_0}\right)^{1/2}. \tag{24}$$

Hence, ε_0 decreases as β increases: $\epsilon_0 \simeq (1 - 2\beta^2)\Delta$ at $\beta \ll 1$ and $\epsilon_0 = \Delta/\beta$, at $\beta \gg 1$. In a weakly-coupled N layer ($\beta \gg 1$) the minigap $\epsilon_0 = \Delta/\beta$ expressed in terms of R_B using equation (23) is independent of superconducting parameters:

$$\epsilon_0 = \frac{\hbar}{4e^2 N_n d R_B}, \qquad \beta \gg 1. \tag{25}$$

The account of the Dynes parameter Γ smoothens the peaks in $N_n(\epsilon)$ and $N_s(\epsilon)$ shown in figure 5 and produces low-energy tails in $N_n(\epsilon)$ extending to the region $0 < \epsilon < \epsilon_0$ of 'mini subgap' states in the N layer [45]. Here, a thin metallic layer can significantly affect $N_n(\epsilon)$ and $N_s(\epsilon)$, resulting in a variety of temperature dependencies of $R_s(T)$.

Shown in figure 6 are the Arrhenius plots of $\ln R_s(T)$ as functions of $\Delta/k_B T$ calculated in [45] for a thin N layer with $\alpha = 0.05$, $\hbar\omega < \Gamma$ and different values of β varying from $\beta = 0.1$ (weak resistive barrier) to $\beta = 30$ (strong resistive barrier). In the limits of $\beta \ll 1$ and $\beta \gg 1$ the qualitative behaviors of $\ln R_s(T)$ are similar to those shown in figure 2: as T decreases, the slope of $\ln R_s(T)$ changes from the bulk Δ at high T to zero at low T, the residual resistance at $\beta \gg 1$ being much larger than at $\beta \ll 1$. The latter reflects higher rf losses in the normal layer as the proximity-induced superconductivity in the N layer weakens with the increase in R_B. As a result, R_i at $\beta \gg 1$ is dominated by the N layer fully decoupled from the S substrate, whereas at $\beta \ll 1$, the N layer is strongly coupled with the S substrate and the structure shown in figure 4 behaves as a single superconductor with an effective Γ. At intermediate values of $\beta = 2\text{–}4$, a change in the slope of $\ln R_s(T)$ occurs around $\Delta/k_B \simeq 8\text{–}10$ due to switching from a thermally activated resistance controlled by the bulk gap Δ at high T to $R_s(T)$ controlled by the smaller minigap ε_0 in the thin N layer. As the temperature decreases further, $R_s(T)$ approaches a temperature-independent residual resistance.

The surface resistance can be reduced by tuning the parameters of the N layer. For example, figure 7 shows $R_s(T, \Gamma, \beta)$ for a thin dirty N layer at two temperatures and different values of Γ. The minimum in $R_s(\beta)$ results from the interplay of two effects. The first one causing the increase of R_s with

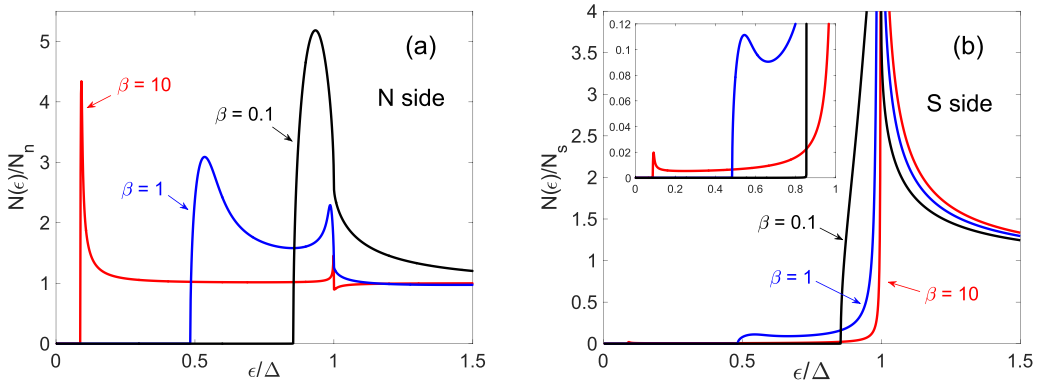

Figure 5. Densities of states at (a) N side and (b) S side of the interface calculated for $\alpha = 0.05$, $\Gamma = 0.05\Delta$, $k_B\Theta = 11\Delta$ and $\beta = 0.1,\ 1,\ 10$, where Θ is the Debye temperature. Inset in (b) shows $N(\epsilon)$ at $\epsilon \ll \Delta$. Reprinted figure with permission from [45], Copyright (2019) by the American Physical Society.

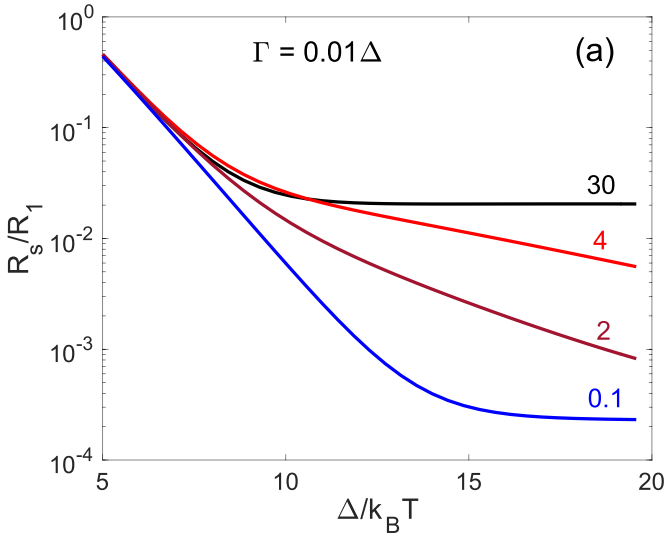

Figure 6. Arrhenius plots calculated for $\alpha = 0.05$ (which corresponds to $d \simeq 1$ nm for Nb), $\lambda = 4\xi_s$, $k_B\Theta = 11\Delta$, $D_n = D_s/3$, $\beta = 0.1,\ 2,\ 4,\ 30$, and $\Gamma = 0.01\Delta$. Here $R_1 = \mu_0^2\omega^2\xi_s\lambda^2/2\rho_s$ and Θ is the Debye temperature. Reprinted figure with permission from [45], Copyright (2019) by the American Physical Society.

β results from decreasing the proximity-induced minigap ε_0 in the N layer as the interface resistance R_B increases. The second effect causing the initial decrease of R_s with β results from the change in the DOS around the N layer, as shown in figure 5. Here, a moderate broadening of the DOS peaks due to the combined effect of finite quasiparticle lifetime $\hbar/\Gamma$ and the metallic layer reduces R_s in a way similar to equation (19). Moreover, in the case of $\Delta/k_BT = 4$ shown in figure 7(a), the minimum in R_s at $\Gamma = 0.01\Delta$ with the N layer is below R_{s0}, suggesting that one can engineer an optimal DOS to reduce R_s below its value for an ideal surface.

3.3. Nonlinear electromagnetic response

The pairbreaking effect of current on the DOS was addressed theoretically in the sixties [19–21, 127] and then observed by tunneling measurements [128]. Shown in figure 8(a) is the DOS in the clean limit $l_i \gg \xi_0$ and $\Gamma = 0$ calculated in [27]. Here, the current turns the DOS singularity at $\epsilon = \Delta$ into a finite peak and reduces the quasiparticle gap ϵ_g at which $N(\epsilon_g) = 0$. The gap $\epsilon_g(J)$ is smaller than Δ and decreases with the current density J, whereas Δ^2 proportional to the superfluid density is *independent* of J at $J < J_g$ and $T = 0$, where $J_g = en_0\Delta_0/p_F$ is the critical current density at which ϵ_g vanishes [19–21]. In a clean superconductor, the gap ϵ_g is anisotropic and depends on the angle between $\mathbf{J}$ and the momentum of a quasiparticle.

In the current-carrying state impurities round the cusps in $N(\epsilon)$ as shown in figure 8(b). Here, the quasiparticle gap decreases as J increases but *remains finite* as J reaches the depairing current density J_c. Thus, impurities preserve the gapped state all the way to the pairbreaking limit, unlike the case shown in figure 8(a). There is a critical concentration of impurities above which the gap ϵ_g at $J = J_c$ opens, so that a superconductor at $J = J_c$ is in the gapless state if $a = \pi\xi_0/l < a_c$ and in a gapped state at $a = \pi\xi_0/l > a_c$. The critical value of $a_c = 0.36$ corresponds to the mean free path smaller than $l_c = \pi\,\xi_0/a_c \approx 8.72\xi_0$ [27]. The dependence of ϵ_g on the mean free path at $a > 0.36$ is shown in figure 8(c). The critical gap $\epsilon_g(a)$ at $J = J_c$ increases monotonically with a and approaches $\epsilon_g(\infty) = 0.323\Delta_0$ at $l_i \ll \xi_0$. Scattering of quasiparticles on impurities makes ϵ_g isotropic and independent of the direction of $\mathbf{J}$.

The dependencies of ϵ_g and Δ on J in the dirty limit are given by [21]

$$\epsilon_g^{2/3} = \Delta^{2/3} - \left(\frac{J}{J_0}\right)^{4/3}\Delta_0^{2/3} \tag{26}$$

$$\Delta(J) = \left(1 - \frac{\pi J^2}{4J_0^2}\right)\Delta_0, \qquad J \ll J_0, \tag{27}$$

where $J_0 = \phi_0/\sqrt{2}\pi\mu_0\lambda^2\xi \sim J_c$. The current-induced DOS broadening makes the surface resistance dependent on J in a way similar to the dependence of R_s on other pairbreaking parameters considered above. At $T \ll T_c$ and $\hbar\omega \ll \Delta$, the exponentially small density of quasiparticles affects neither T_c nor the dynamics of the superconducting condensate, but

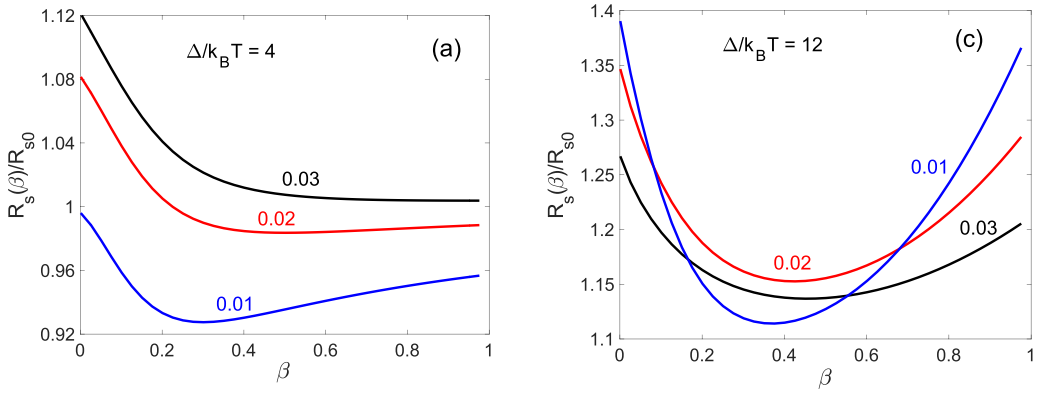

Figure 7. Minima in $R_s(\beta)$ as a function of the interface barrier parameters β calculated at $\Delta/k_BT = 4,\ 8,\ 12,\ 20$, $\Gamma = 0.01,\ 0.02,\ 0.03$, $\lambda = 4\xi_S$, $D_n = 0.1D_s$, $\alpha = 0.05$, and $k_B\Theta = 11\Delta$. Here $R_s(T,\beta,\Gamma)$ are normalized to their respective values $R_{s0}(T,\Gamma)$ for each Γ in the absence of the N layer and Θ is the Debye temperature. Reprinted figure with permission from [45], Copyright (2019) by the American Physical Society.

the rf superflow causes temporal oscillations of the DOS and $\epsilon_g(t)$, resulting in a field dependence of $R_s(B_a)$. Usually, R_s is expected to increase with the rf field due to current pair-breaking, electron overheating, penetration of vortices, etc [14, 129]. Yet, a significant reduction of R_s by the rf field has been observed in alloyed Nb cavities [33–41] in which the decrease of R_s by $\simeq$20%–60% at 2 K extends to the fields $B_a \simeq$ 90–100 mT at which the density of screening currents at the surface reaches $\simeq$50% of the pairbreaking limit, $J_c \simeq B_c/\mu_0\lambda$. The reduction of R_s by a microwave field is not unique to Nb: similar effects have been observed in thin films [130–132]. Particularly, a reduction of $R_s(B_0)$ with the dc field B_0 superimposed onto a low-amplitude rf field in Pb, Sn, Tl, and Al has been known since the fifties [133–139].

The microwave suppression of R_s can be understood as follows [44]. The rf field $B(t) = B_a\cos\omega t$ causes temporal oscillations of the DOS between the singular $N(\epsilon)$ at $B(t) = 0$ to a broadened $N(\epsilon, B_a)$ at the peak field $B(t) = B_a$, as shown in figure 8. Thus, the peak in the DOS $\langle N(\epsilon)\rangle$ averaged over the rf period is smeared out within the energy range $\epsilon_g < \epsilon < \Delta_0$. In the dirty limit equation (26) yields the width of the averaged gap peak $\delta\epsilon = \Delta_0 - \epsilon_g \sim (B_a/B_c)^{4/3}\Delta_0$ at $B_a \ll B_c$. As a result, the current-induced broadening of the DOS can be roughly accounted for by replacing the materials-related broadening parameters Γ or Γ_p with the current-induced broadening $\delta\varepsilon$ in equation (19). This yields a logarithmic decrease of R_s with B_a:

$$R_s(B_a) \sim \frac{\mu_0^2\omega^2\lambda^3\Delta}{\rho_n k_B T}\ln\left[\frac{CTB_a^{4/3}}{T_cB_c^{4/3}}\right]e^{-\Delta/k_BT}, \qquad (28)$$

where $C \sim 1$. This qualitative picture gives an insight into a mechanism of microwave reduction of $R_s(B_a)$ in the region of the parameters $(\Gamma/\Delta)^{3/4}B_c \ll B_a \ll B_c$ and $\max(\Gamma, \hbar\omega) \ll k_BT$ relevant to the experiments [33–40]. The behavior of $R_s(B_a)$ is affected by material treatments, yet the qualitative equation (28) describes well $Q(B_a)$ observed on Ti-doped Nb cavities [35]. The effect of current-induced DOS broadening on R_s was pointed out by Garfunkel [140] who calculated $R_s(H)$ was biased by a strong parallel dc field H in the BCS clean limit.

A theory of nonlinear surface resistance $R_s(B_a)$ in strong microwave fields must take into account both the temporal DOS oscillations and nonequilibrium effects [83, 141–144]. Many previous works have focused on nonequilibrium states caused by absorption of high-frequency photons at weak fields $B_a \ll (\omega/\Delta)^{3/4}B_c$ and $\hbar\omega > k_BT$ for which the effect of rf current on $N(\epsilon)$ is weak [145–147]. In this case $\sigma_1(B_a)$ can decrease with B_a as the quasiparticle population spreads to higher energies $\epsilon > k_BT$ [132]. This mechanism is similar to that of stimulated superconductivity [148, 149] and can explain the reduction of σ_1 with B_a observed in Al films at 5.3 GHz at 350 mK [132]. However, this approach is not applicable to low-frequency and high-amplitude rf fields with $\hbar\omega \ll k_BT$ and $B_a > (\omega/\Delta)^{3/4}B_c$ for which $R_s(B_a)$ is determined by the time-dependent DOS and a nonequilibrium distribution function $f(\epsilon,t)$ driven by an oscillating superflow. A nonlinear surface resistance $R_s(B_a)$ in the dirty limit and $\lambda \gg \xi$ and $\hbar\omega \ll k_BT$ was calculated in [150] by solving the time-dependent Usadel equations, taking into account temporal oscillations of $N(\epsilon,t)$, $\epsilon_g(t)$ and $f(\epsilon,t)$ under strong rf field. Here R_s is obtained from the relation $H_a^2R_s/2 = \int_0^\infty\langle J(A(x,t)E(x,t)\rangle dx$, where $J[A(x,t)]$ is the current density calculated for exact solutions of the Usadel equations, $\langle\ldots\rangle$ denotes averaging over rf period and $E(x,t) = -\dot{A} = B_a\omega\lambda e^{-x/\lambda}\sin\omega t$. This theory, in which $R_s(B_a)$ can decrease with B_a even for the equilibrium Fermi distribution of quasiparticles, captures the field dependence of $R_s(B_a)$ observed on Nb cavities [33–41].

Strong rf fields can drive quasiparticles out of thermodynamic equilibrium making $f(\epsilon,t)$ different from the Fermi–Dirac distribution $f_0(\epsilon) = (e^{\epsilon/k_BT}+1)^{-1}$. Generally, $f(\epsilon,t)$ is determined by kinetic equations taking into account the current pairbreaking and scattering of quasiparticles on phonons and impurities [83]. The deviation from equilibrium depends upon the rate $1/\tau_\epsilon$ with which the rf power absorbed by quasiparticles is transferred to the crystal lattice. The time τ_ε is determined by inelastic scattering of quasiparticles on

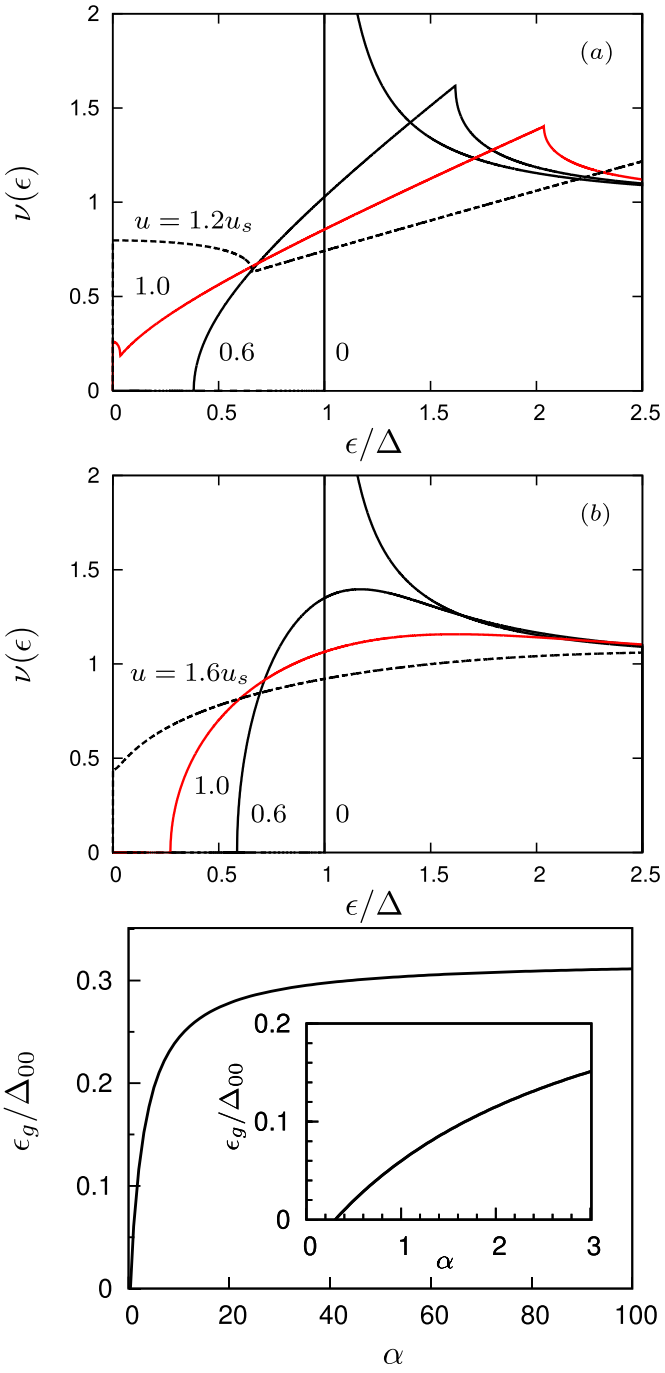

Figure 8. Effect of Meissner current on the normalized density of states $\nu(\epsilon) = N(\epsilon)/N_n$ at different ratios H/H_s for: (a) clean limit at $a = 0$, (b) dirty limit at $a = 3.6$. The red lines show $\nu(\epsilon)$ at the superheating field. Dependence of the quasiparticle gap on the mean free path (c). Reprinted figure with permission from [27], Copyright (2012) by the American Physical Society.

phonons and recombination of quasiparticles into Cooper pairs [102]. If $\omega\tau_\epsilon \ll 1$, quasiparticles adiabatically follow the temporal DOS oscillations so $f(\epsilon,t) \to f_0(\epsilon)$, but the density of quasiparticles $n(t) = 2\int_0^\infty f_0(\epsilon)N[\epsilon,J(t)]d\epsilon$ varies in response to the instant changes of $N[\epsilon,J(t)]$ shown in figure 8. If $\omega\tau_\epsilon \gg 1$, quasiparticles do not have enough time to equilibrate so their density does not change much during rapid oscillations of $N(\epsilon,t)$. Due to slow power transfer between electrons and phonons at $\omega\tau_\epsilon \gg 1$, quasiparticles become hotter than the lattice, at it has been established in thin film electronic applications, for example, superconducting bolometers [151].

The rf periods ∼0.1–1 ns are typically much longer than the electron–electron scattering time τ_{ee} and the condensate relaxation time $\tau_\Delta \sim \hbar/\Delta$. In this case, the quasiparticle energy relaxation time τ_ε is limited by inelastic electron–phonon collisions for which $\tau_\epsilon(T)$ at $T \approx T_c$ is given by [83]:

$$\tau_\epsilon = \frac{8\hbar}{7\pi\zeta(3)\gamma k_B T_F}\left(\frac{c_s}{v_F}\right)^2\left(\frac{T_F}{T}\right)^3. \qquad (29)$$

Here γ is the electron–phonon coupling constant, c_s is the speed of longitudinal sound, $T_F = \epsilon_F/k_B$ is the Fermi temperature and $\zeta(3) \approx 1.2$. The time $\tau_\epsilon(T)$ increases rapidly as T decreases. For Nb_3Sn with $c_s/v_F \simeq 10^{-3}$, $T_F \sim 10^5$ K, $T_c = 17$ K and $\gamma \simeq 1.5$ [152], equation (29) yields $\tau_\epsilon \sim 10$ ps at T_c and $\tau_\epsilon \sim 6$ ns at 2 K. Hence Nb_3Sn at 1 GHz is in a quasi-equilibrium state near T_c but can be in a non-equilibrium state at 2 K. For Al with $c_s \simeq 5.1$ km s^{-1}, $v_F \simeq 2030$ km s^{-1}, $T_F = 1.36\times10^5$ K, $T_c = 1.2$ K and $\gamma = 0.43$, [84, 153], one obtains $\tau_\epsilon \sim 0.4\,\mu$s at T_c. Generally, τ_ε depends on energy ε, which becomes essential at low temperatures [102]. The electron–phonon relaxation time τ_ε can be reduced by nonmagnetic and magnetic impurities [154–156] or by a thin proximity coupled metallic suboxide layer which reduces the minigap at the surface and allows more effective energy transfer from the quasiparticles to phonons. These effects can expand the temperature range of the quasi-equilibrium state.

The nonlinear conductivity controlled by the nonequilibrium kinetics of quasiparticles in strong electromagnetic fields is beyond the scope of this review. Here, we focus on the field dependence of R_s due to the temporal current broadening of the DOS affected by the Dynes parameter Γ, magnetic impurities or a proximity coupled N layer at quasi-equilibrium, $\omega\tau_\epsilon < 1$. Interplay of the current and material broadening of the DOS can produce a multitude of field dependencies of $R_s(B_a)$ [45, 46, 157–160]. Unlike the Dynes parameter in the bulk, tuning the layer thickness d and conductivity σ_n of the metallic suboxide, the contact resistance R_B and the bulk conductivity σ_s by material treatments can be used to optimize $R_s(B_a)$.

Shown in figure 9 are examples of $R_s(B_a)$ curves calculated in [46] for different thicknesses of the N layer and two interface barrier parameters $\beta = 0.1$ and $\beta = 1$ being around the minimum of R_s in figure 7. The dashed line shows the microwave suppression of $R_s(B_a)$ caused by the current broadening of the DOS for an ideal surface with $d = 0$ [44]. For $\beta = 0.1$, the dip in $R_s(B_a)$ gets less pronounced as the N layer thickness increases, $R_s(B_a)$ increasing with field at $\alpha > 0.1$. This is consistent with weakening the induced superconductivity and reduction of the minigap in the N layer as it becomes thicker. Yet the crossover of $R_s(B_a,\alpha)$ curves at low fields in figure 9(a) implies that removing the N layer increases $R_s(B_a)$,

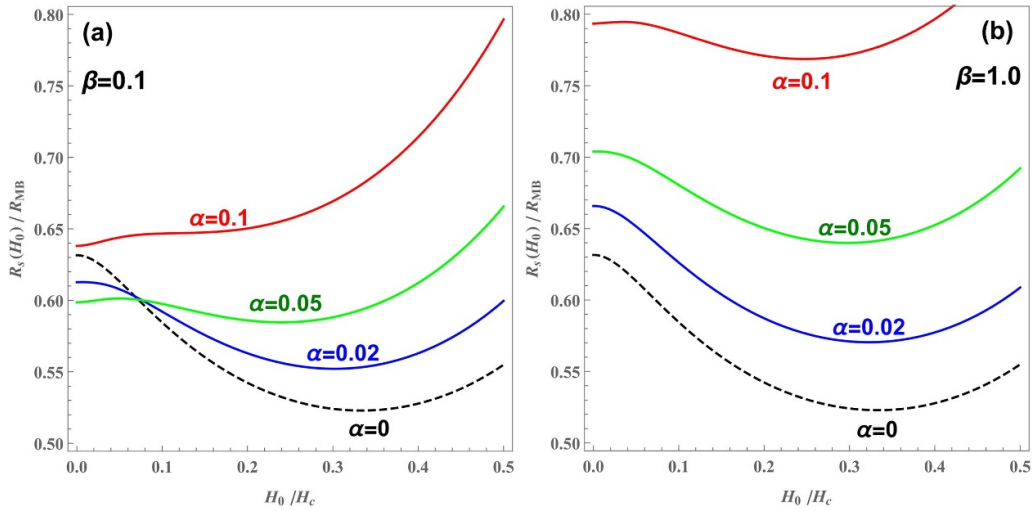

Figure 9. $R_s(H_0)$ as a function of the field amplitude H_0 calculated at different N layer thicknesses: $\alpha = 0.02, 0.05, 0.1, 0.2$, $\beta = 0.1, 1.0$, $\Gamma_n/\Delta = \Gamma_s/\Delta = 0.005$, $\Gamma_p = 0$, $k_B\Theta = 11\Delta$, $D_n = 0.5D_s$, $\lambda = 10\xi_s$, $\omega/\Delta = 0.001$, and $T/\Delta = 0.11$, where Θ is the Debye temperature. The dashed line shows $R_s(H_0)$ calculated for $d = 0$, $\Gamma/\Delta = 0.005$. All $R_s(H_0)$ curves are normalized to the ideal BCS surface resistance R_{MB} at $\Gamma = 0$. Reprinted figure with permission from [46], Copyright (2019) by the American Physical Society.

in agreement with figure 7. This crossover disappears at a larger contact resistance as shown in figure 9(b).

Figure 10 shows how the field dependence of $R_s(B_a)$ changes as the conductivity ratio σ_n/σ_s is varied at a fixed thickness of the N layer for three values of the interface barrier parameter β [45]. Given that R_B and σ_n/σ_s can be changed significantly by heat treatments [122–124] and alloying with nonmagnetic impurities, the results shown in figures 9 and 10 may account for the variability of the Q-factors of Nb cavities.

3.4. Tuning R_s by alloying

Reduction of microwave losses by optimizing the DOS using pairbreaking effects may shed light on the mechanisms behind the improvement of the rf performance of Nb cavities after a low-temperature baking (by 100 °C–200 °C for 2 h) [28–32], medium temperature baking at 290 °C–390 °C for 3 h [32], high-temperature (800 °C) annealing [7] and infusion of Nb with impurities. The latter has caused much interest since the discovery of microwave reduction of $R_s(B_a)$ after alloying the Nb cavities with nitrogen, titanium, oxygen and other impurities [33–41]. Alloying with nonmagnetic impurities could reduce the high-field rf losses since the quasiparticle gap ϵ_g which ensures an exponentially small R_s does not close up to $B_a = B_s$. This may also pertain to the baking effect, which reduces the high-field Q-slope by diffusive redistribution of impurities, particularly interstitial oxygen or hydrogen in a thin ∼20 nm layer at the surface [28–32]. The length $L = (Dt)^{1/2}$ over which impurities diffuse from the oxide surface layer to the bulk during the time t gives $L \simeq 17$ nm for the interstitial oxygen at 120 °C and $t = 48$ h taking the diffusivity D from [161]. Uncovering the mechanisms by which material treatments affect superconducting properties requires compositional analysis of the Nb surface using multiple tools such as transmission electron microscopy (TEM), Auger electron spectroscopy (AES), x-ray photoelectron spectroscopy (XPS), electron energy loss spectroscopy (EELS) and atom probe microscopy [8, 162–169] combined with STS and $Q(B_a)$ measurements to reveal the effects of different treatments on the DOS and R_s.

There are several scenarios by which the infusion of impurities over a few μm from the surface could contribute to the field-induced reduction of $R_s(B_a)$. 1. Impurities mostly reduce the DOS broadening in the entire layer of rf field penetration $\simeq 2\lambda \sim 100$ nm, which reveals the microwave reduction of $R_s(B_a)$ of the BCS model [44, 150]. 2. The impurity infusion primarily modifies the surface oxides, for instance, by shrinking the metallic suboxide layer [44]. 3. The appearance of magnetic impurities and TLSs in the oxide layer and N–S interface [5, 108, 109, 170]. To determine which of these scenarios is more relevant, the R_s measurements are to be combined with scanning tunneling spectroscopy (STS) to measure the DOS at the surface and link it with the behavior of $R_s(B_a)$. This has been implemented by several groups, starting with the pioneering work [33] which showed that Ti infusion significantly reduces the lateral distribution of local values of Δ. The effect of N-doping on the DOS at the Nb surface was addressed in [120, 121]. In particular, the analysis of STS spectra in [121] using the model of [45] gave an insight into the effect of N infusion on the properties of the metallic suboxide.

The results of [121] summarized in figure 11 indicate that the effect of the nitrogen infusion gives rise to the following: 1. Slightly reduces the average superconducting gap $\bar{\Delta}$ while significantly reducing the spatial inhomogeneities of Δ and the Dynes parameter Γ. 2. Reduces the thickness of metallic suboxide from ≈2 nm down to ≈1.2 nm. 3. Reduces spatial inhomogeneities of the Nb suboxide thickness and the interface contact resistance parameter β close to the optimal values

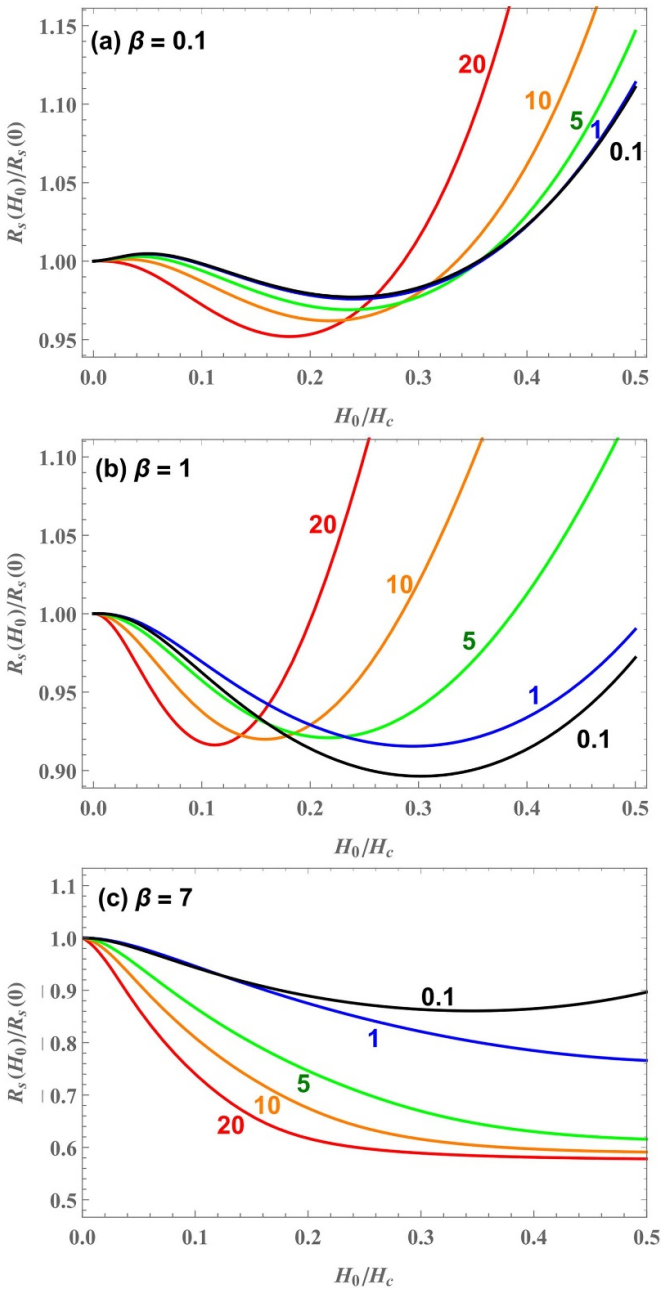

Figure 10. $R_s(H_0)$ as a function of the rf amplitude H_0 calculated for $D_n/D_s = 0.1, 1, 5, 10, 20$, $\alpha = 0.05$, $\beta = 0.1, 1, 7$, $\Gamma_n = \Gamma_s = 0.005\Delta$, $\Gamma_p = 0$, $k_B\Theta/\Delta = 11$, $\lambda = 10\xi_s$, $\hbar\omega/\Delta = 0.001$, and $k_BT/\Delta = 0.11$, where Θ is the Debye temperature. Reprinted figure with permission from [46], Copyright (2019) by the American Physical Society.

0.3–0.4 corresponding to a minimum R_s shown in figure 7. It seems that these effects of the nitrogen doping bring the DOS toward its optimum which minimizes R_s, while reducing the effect of such extrinsic factors as the lateral inhomogeneity of superconducting parameters characteristic of the surface of Nb resonators.

Material mechanisms which cause the modifications of the oxide structure in Nb require further investigations. It was found that heat treatment in a temperature range sufficient to dissociate the natural surface oxide not only causes a significant reduction of the residual resistance down to $R_i \simeq 1$ nΩ but also reduces the thermally-activated BCS part of R_s [32]. This observation seems consistent with the theoretical results of [45] which show that both R_i and R_{BCS} can be reduced if d_n and R_B are reduced from their respective values on the right side of the minimum in figure 9. Furthermore, recent TEM investigations indicate that nitrogen doping passivates the Nb surface by introducing a compressive strain close to the Nb/air interface, which impedes the diffusion of oxygen and hydrogen atoms and reduces the surface oxide thickness [169]. This conclusion seems consistent with the analysis of STM data shown in figure 11.

4. Dielectric losses and kinetic inductance

This section focuses on two contributions to the electromagnetic response not related to quasiparticles. The first one gives rise to a microwave suppression of the residual surface resistance due to two level states (TLS), and the second one pertains to tuning the kinetic inductance of N-S bilayers and nanowires by the proximity effect.

4.1. TLSs

Microwave losses in amorphous dielectrics at low temperatures can be dominated by the presence of TLS in the material [60, 61]. These defects exist in a glassy state in which light atoms or trapped electrons or dangling atomic bonds can tunnel between two neighboring positions in a disordered atomic structure. Such TLS can occur in amorphous oxide layers on the surface of Al and Nb as well as at interfaces between a superconducting film and a dielectric substrate. TLS have attracted much attention as a source of noise and decoherence in superconducting quantum devices at low temperatures. Here, TLS can not only contribute to the residual surface resistance but also result in decreasing $R_i(E)$ with the rf electric field E [108, 109, 170, 171]:

$$R_i^{TLS}(E) = R_{i0}^{TLS}\frac{\tanh(\hbar\omega/2k_BT)}{[1+(E/E_c)^2]^q}, \tag{30}$$

where q is close to $1/2$ in the standard tunneling model [60, 61], although the q values well below $1/2$ have also been observed [170]. The factor R_{i0}^{TLS} is proportional to the TLS density of states and depends on the resonator geometry, $E/E_c = \omega_R\sqrt{\tau_1\tau_2}$, where $\omega_R = 2d_0E/\hbar$ is the Rabi frequency, $d_0 \simeq ea_0$ is a dipole moment proportional to the tunneling distance a_0, and $\tau_1(T)$ and $\tau_2(T)$ are the TLS energy relaxation and dephasing times, respectively. One can see that $R_i^{TLS}(E)$ decreases with E at $E > E_c = \hbar\sqrt{\tau_1\tau_2}/2d_0$ as the TLS becomes saturated by the microwave field.

TLS losses in superconducting films can depend strongly on the dielectric substrate, for instance, the losses in Nb on SiO_2 are significantly higher than in Nb on Al_2O_3 [61]. Of particular interest are intrinsic TLS losses coming from the native oxides in Nb or Al separated from the losses in external dielectric components [172–174]. Fitting $R_i(B_a)$ measured on

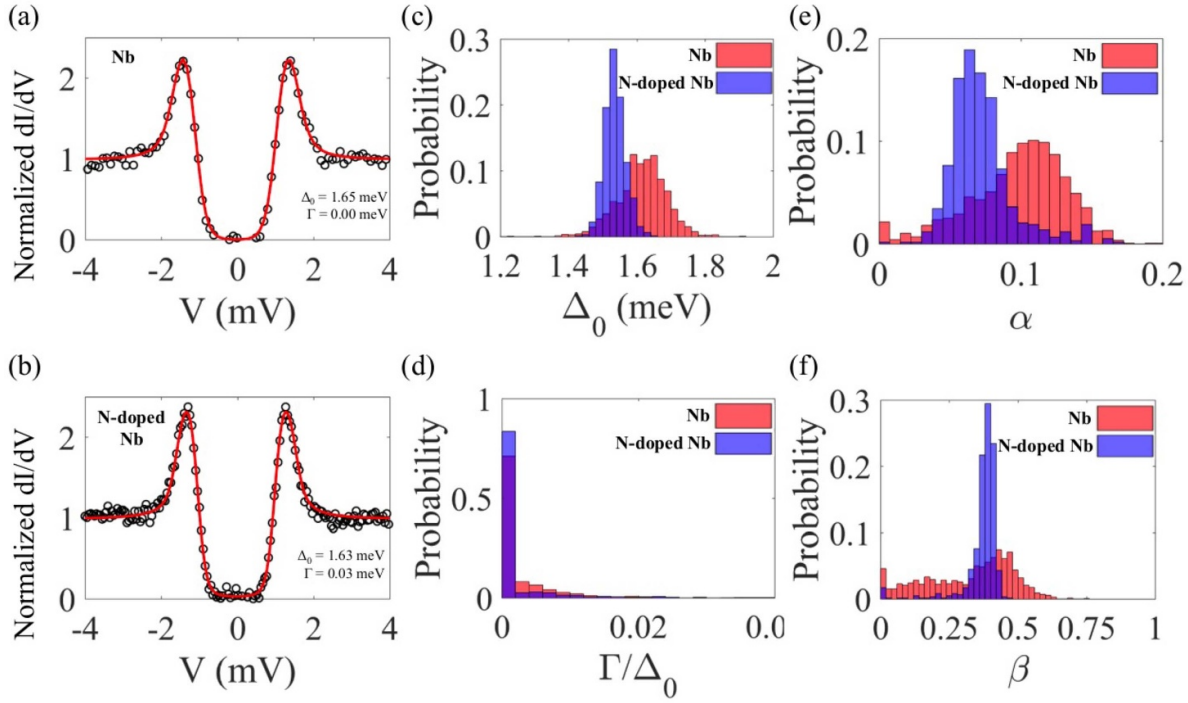

Figure 11. Typical tunneling spectra (dots) acquired on Nb and N-doped Nb surfaces. The red lines are the fits with the model of [45]. (c), (d) Histogram comparison of the fit parameters Δ_0 and Γ/Δ_0 respectively. (e), (f) Histogram comparison of the fit parameters α and β respectively. For Nb samples, the number of spectra analyzed is $N = 1440$ (red) and for N-doped samples $N = 576$ (blue). Spectra were taken 32.6 nm away from each other at $T = 1.5$ K. Reprinted figure with permission from [121], Copyright (2020) by the American Physical Society.

Nb cavities at 1.5–2 K and 1.3 GHz with equation (30) gave $E_c \approx 0.2\,\mathrm{MV\,m^{-1}}$ [109], much higher than the parallel electric field at the equatorial cavity surface $E \simeq \omega B_a \lambda \simeq 3 \times (10^{-2}$–$1)\,\mathrm{V\,m^{-1}}$ at $B_a = 0.1$–10 mT. The decrease of $R_i(B_a)$ with B_a observed in [109] was attributed to TLS on the inner cavity surfaces near the orifices, where the perpendicular rf electric field can reach a few $\mathrm{MV\,m^{-1}}$. Yet, a much lower $E_c \simeq 56\,\mathrm{V\,m^{-1}}$ was observed on a 150 nm thick Nb stripline resonator grown on a Si substrate and coated with aluminum oxide [108].

TLS in AlO_x or Nb_2O_5 oxides have been commonly associated with dangling atomic bonds and oxygen vacancies [173, 174], although the true atomic origin of TLS has not been fully understood [61]. TLS may also result from common environmental impurities, such as nitrogen, carbon or hydrogen, which get dissolved in the material during the film growth and deposition [8]. For instance, the formation of metallic hydride precipitates in Nb and their contribution to rf losses is well-known [8, 110–114]. If the hydrogen bound to the oxygen vacancy in Nb_2O_5 does behave as TLS [175], one may expect R_i to increase after neutron or proton irradiation [176] which produces hydrogen irradiation defects and lattice disorder. In any case, the manifestations of TLS and quasiparticle contributions to the surface resistance are quite different. At GHz frequencies and $T = 1$–2 K the TLS residual resistance $R_i^{\mathrm{TLS}} \propto \tanh(\hbar\omega/2k_\mathrm{B}T)$ increases with ω and becomes independent of T at mK temperatures. This distinguishes the TLS microwave reduction of $R_i^{\mathrm{TLS}}(B_a)$ from that of the quasiparticle surface resistance $R_s \propto \exp(-\Delta/k_\mathrm{B}T)$ which decreases exponentially as T decreases.

4.2. Tuning the kinetic inductance by the proximity effect

In addition to the reduction of dissipative conductivity σ_1, the proximity effect can be used to tune the inductive conductivity σ_2 and either increase or decrease the kinetic inductance L_k which defines the energy $L_k I^2/2$ of flowing supercurrent I. Here, large L_k is desirable in transmons [1] and kinetic inductance photon detectors [2–5], whereas small L_k can be useful to reduce the readout or reset times $\tau_r = L_k/R_0$ in quantum memories, qubits and photon detectors, where R_0 is the resistance of the readout circuit. The influence of the proximity effect on L_k is most transparent for thin-film S-N bilayers or nanowires, which have been used in single photon detectors [177–179].

Consider an N-S bilayer shown in figure 4 with the thicknesses d_n and d_s smaller than the respective coherence lengths ξ_n and ξ_s. This corresponds to the Cooper limit [180, 181] in which the superconducting order parameters $\psi_{N,S}$ are uniform through the N and S layers, although ψ_N can be different from ψ_S due to the decoupling effect of R_B. Such N-S bilayers have been studied in the literature (see e.g., a review [182] and the references therein). In the case of $R_B = 0$ and $\Gamma \ll k_\mathrm{B}T_c$ the critical temperature of the bilayer decreases exponentially with the N layer thickness [180]:

$$T_c = T_{c0} \exp\left(-d_n N_n/\gamma_s d_s N_s\right), \tag{31}$$

where $T_{c0} = 1.13\Theta \exp(-1/\gamma_s)$ is the critical temperature of the S layer, γ_s is the BCS pairing constant and Θ is the Debye temperature. At $R_B = 0$ a dirty N-S bilayer has a

uniform superconducting order parameter determined by the Usadel equation (22) with $\Gamma_p = 0$, $\epsilon \to \epsilon + i\tilde{\Gamma}$ and the composite parameters [183]:

$$\tilde{\Delta} = \frac{d_s N_s \Delta_s + d_n N_n \Delta_n}{d_s N_s + d_n N_n}, \quad \tilde{\Gamma} = \frac{d_s N_s \Gamma_s + d_n N_n \Gamma_n}{d_s N_s + d_n N_n}. \tag{32}$$

The pairing potential Δ_s is nonzero in the S layer and vanishes ($\Delta_n = 0$) in the N layer [181, 182]. The composite $\tilde{\Delta}$ is determined by the BCS gap equation with the effective coupling constant

$$\tilde{\gamma} = \frac{d_s N_s \gamma_s + d_n N_n \gamma_n}{d_s N_s + d_n N_n}. \tag{33}$$

Equations (32) and (33) describe both the N-S bilayer with $\gamma_n = \Delta_n = 0$ and a bilayer of two different superconductors S and S′ for which the index n refers to the S′ layer with nonzero γ_n and Δ_n. For the N-S bilayer with $\tilde{\Gamma} \ll k_B T_c$, equation (33) yields equation (31) because $T_c = 1.13\Theta \exp(-1/\tilde{\gamma})$ and $\gamma_n = 0$. Unlike the dissipative conductivity σ_1, the effect of weak Dynes broadening of the DOS on σ_2 and L_k is negligible [183].

The current I flowing along a strongly coupled bilayer of width $w \ll \lambda_s^2/d_s$ in response to the vector potential A is a sum of phase-locked currents in both films: $I = -\mu_0 w \left(d_n/\lambda_n^2 + d_s/\lambda_s^2\right) A$, where $\lambda_{s,n}^{-2} = (\pi \mu_0 \sigma_{s,n} \tilde{\Delta}/\hbar) \tanh(\tilde{\Delta}/2k_B T)$ in the dirty limit [183]. The kinetic inductance per unit length $L_k = -A/I$ is then:

$$L_k = \frac{\hbar \coth(\tilde{\Delta}/2k_B T)}{\pi w \tilde{\Delta}(d_s \sigma_s + d_n \sigma_n)} \tag{34}$$

For a single S film, equation (34) yields $L_{k0} = \mu_0 \lambda_s^2/w d_s$ [5].

Deposition of the N layer can either decrease or increase L_k. Shown in figure 12 is $L_k(d_n)$ calculated from equation (34) for different diffusivity ratios $D_n/D_s = \sigma_n N_s/\sigma_s N_n$ at $\gamma_s = 0.5$, $T \ll T_c$ and $\tilde{\Delta}(d_n) = 1.74 k_B T_c(d_n)$, where $T_c(d_n)$ is given by equation (31). If $D_n < D_s/\gamma_s$ the kinetic inductance monotonically increases with d_n due to suppression of T_c by the proximity effect. For a more conductive N layer with $D_n > D_s/\gamma_s$ the dependence of L_k on d_n becomes nonmonotonic due to the interplay of two effects: 1. The decrease of L_k with d_n due to the additional inertia of Cooper pairs induced in the N layer (the term $d_n \sigma_n$ in the denominator of equation (34)). 2. The increase of L_k with d_n due to the proximity effect reduction of $T_c(d_n)$. If $D_n \gg D_s$ the optimum thickness $\tilde{d}_n$ and the minimum inductance $\tilde{L}_k$ at $d_n = \tilde{d}_n$ are given by:

$$\tilde{d}_n \simeq d_s \frac{\gamma_s N_s}{N_n}, \qquad \tilde{L}_k \simeq \frac{3 L_{k0} D_s}{\gamma_s D_n} \ll L_{k0}. \tag{35}$$

Deposition of highly conductive Ag or Cu films onto a superconducting film can significantly decrease L_k. For instance, a thin Cu film of thickness $d_n = \tilde{d}_n$ on top of a NbN film could decrease L_k at $J \ll J_d$ by some two orders of magnitude because $\sigma_{NbN}/\sigma_{Ag} \sim 10^{-2} - 10^{-3}$. The effect of the mean free path and subgap states on L_k was investigated in [160]. Increasing the contact resistance weakens the S-N proximity coupling and reduces the contribution of the N layer to the kinetic inductance, so that $L_k \to L_{k0}$ at $\beta \gg 1$. Both $\sigma_2(J)$ and $L_k(J)$ increase with J due to current pairbreaking [5, 157, 160, 184, 185], which manifests itself in a nonlinear Meissner effect and intermodulation [129, 186–188]. Nonlinear screening of a dc parallel field and the breakdown of superconductivity in N-S bilayers has been investigated in [189–192].

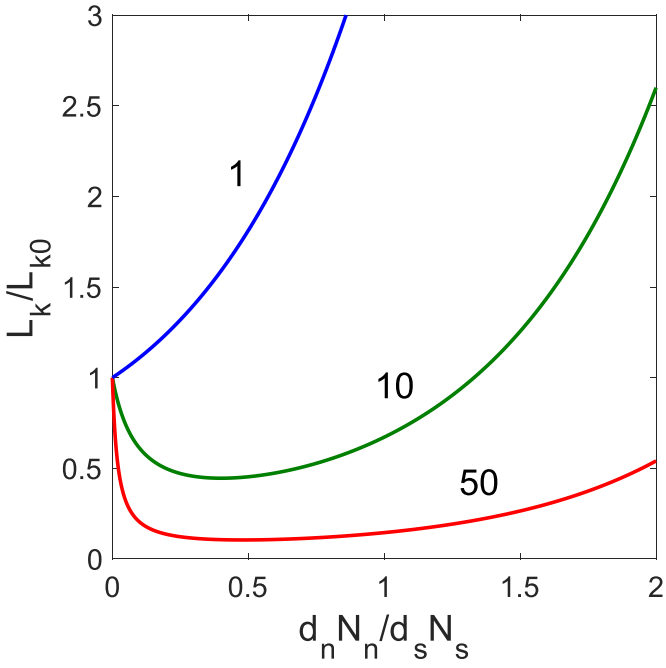

Figure 12. The kinetic inductance of an N-S bilayer as a function of the N layer thickness calculated from equation (34) at $\gamma_s = 0.5$, $T \ll T_c(d_n)$ and different diffusivity ratios $D_n/D_s = 1, 10, 50$.

The kinetic inductance can increase greatly in polycrystalline films with weak-linked grain boundaries, particularly granular Al films which have been used in transmons and photon detectors [193–195]. Weakly-coupled grain boundaries characteristic of polycrystalline Nb_3Sn [54–56] can increase L_k and amplify the nonlinear Meissner effect in Nb_3Sn coplanar thin film resonators [196]. Here, a polycrystalline film can be regarded as a network of weakly-coupled planar Josephson junctions, each of which adds a nonlinear kinetic inductance $L_J = \phi_0/2\pi I_c \cos\chi$ inversely proportional to the tunneling Josephson critical current I_c and dependent on the superconducting phase difference χ on the junction [197].

5. Dynamic superheating field

The Meissner state becomes unstable as the applied magnetic field H exceeds a dc superheating field $H_s(T)$ at which a transition to a dissipative state occurs. In type-II superconductors with $\kappa > 1/\sqrt{2}$, the superheating field lies between the lower critical field $H_{c1}(T) = (\phi_0/4\pi\mu_0\lambda^2)[\ln\kappa + c(\kappa)]$ and the upper critical field $H_{c2}(T) = \phi_0/2\pi\mu_0\xi^2$. Here $c(\kappa) \approx 1/2 + (1 + \ln 2)/(2\kappa - \sqrt{2} + 2)$ which approximates the GL calculations better than 1% [198] decreases from $c \approx 1.35$ at $\kappa = 2^{-1/2}$ to $c \to 1/2$ at $\kappa \gg 1$. At $H_{c1} < H < H_{c2}$ a

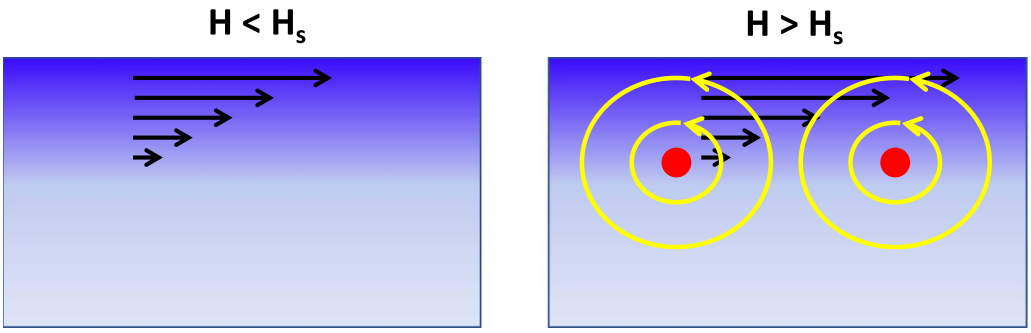

Figure 13. An illustration of how penetration of vortices at $H > H_s$ prevents the breakdown of superconductivity by Meissner current. Left: screening Meissner currents at H slightly below H_s. Right: counterflow produced by penetrating vortices against the screening currents at H slightly above H_s. Vortex cores are shown using red dots.

superconductor is in a metastable state because the Bean–Livingston barrier prevents penetration of vortices through an ideal surface [22]. Clean Nb is a marginal type-II superconductor with $\kappa \approx 0.85$, $B_{c1}(0) \approx (\ln\kappa + c)B_c/\kappa\sqrt{2} \approx 180$ mT and the thermodynamic critical field $B_c(0) \approx 204$ mT [48, 49, 84], where $B_c(T) = \phi_0/2^{3/2}\pi\lambda\xi$ at $T \approx T_c$ and $B_c(0) = (\mu_0 N_s)^{1/2}\Delta_0$. In the BCS model, electron scattering on nonmagnetic impurities increases H_{c2}, does not affect H_c and decreases H_{c1} [18]. In the case of an anisotropic Fermi surface, impurity scattering decreases T_c and H_c [90].

The GL calculations of H_s at $T \approx T_c$ [24, 25] have shown that $H_s(\kappa)$ decreases monotonically with κ from $H_s = 2^{-1/4}\kappa^{-1/2}H_c$ at $\kappa \ll 1$ to $H_s \approx 1.2H_c$ at $\kappa \approx 1$ and to $H_s = (\sqrt{5}/3)H_c$ at $\kappa \gg 1$. The superheating field at $T \ll T_c$ has usually been evaluated by extrapolating the GL results to low temperatures, where the GL theory is invalid. Microscopic calculations of $H_s(T)$ in the entire range $0 < T < T_c$ have only been done for $\kappa \to \infty$ in which case $H_s = 0.84H_c$ at $T = 0$ exceeds the GL extrapolation $H_s = 0.745H_c$ [23]. Calculations of $H_s(T)$ using the Eilenberger equations in the clean limit revealed a maximum in $H_s(T)$ at low T [26], indicating that $H_s(T)$ at low T can hardly be extrapolated from the GL results near T_c. Furthermore, the effect of impurities on $H_s(T)$ at $T \ll T_c$ is different from the GL results at $T \approx T_c$, particularly in the clean limit in which the Meissner currents do not affect λ until the superfluid velocity $v_s = J/n_s e$ reaches the critical value, $v_s = v_c = \Delta_0/p_F$ [19–21]. If $\kappa \gg 1$ and $T = 0$ the gap ϵ_g closes at the field $H_g(2/3)^{1/2}H_c \approx 0.816H_c < H_s$ [19, 27].

The effect of nonmagnetic and magnetic impurities on $H_s(T)$ calculated from the Eilenberger equations at $\kappa \gg 1$ and $0 < T < T_c$ was addressed in [27]. The results show that nonmagnetic impurities do not affect H_s near T_c where $H_s = 0.745H_c$. At low temperatures $H_s(a)$ has a small maximum as a function of the impurity parameter $a = \pi\xi_0/l_i$, the maximum in $H_s(a)$ washes out as T decreases. The effect of nonmagnetic impurities on H_s at $\kappa \gg 1$ is weak: H_s varies from $0.84H_c$ in the clean limit $(a = 0)$ to $H_s \simeq 0.812H_c$ in the dirty limit $(a = 20)$. In contrast, pairbreaking magnetic impurities diminish T_c and H_s [27]. The effect of subgap states on H_s was calculated in [157, 159, 160]. The full temperature dependence of the dc depairing current density $J_c(T, l_i)$ was calculated both from the Eilenberger equations for arbitrary mean free path [199] and from the Eliashberg equations [200].

An important question is whether the dc superheating field is the true field limit of the Meissner state under strong microwaves [201]. The answer depends on the relation between the time formation of the vortex core τ_v and the rf period: if $\nu\tau_v \gg 1$ vortices do not have enough time to form, then the dynamic superheating field H_d may exceed the static H_s. The core formation time τ_v can be evaluated as $\tau_v \sim \xi/v_d \simeq (v_F/\pi v_d)\hbar/\Delta$, where v_d is the terminal velocity of a vortex penetrating through the surface at $H = H_s$. Measurements of v_d in Pb [202] and Nb-C [203] gave $v_d \sim 10$–20 km s^{-1}. Taking $\xi \sim 40$ nm for Nb yields $\tau_v \sim (2$–$4) \times 10^{-12}$ s and $\nu\tau_v \sim 10^{-2}$–10^{-3} at GHz frequencies. In this case, penetration of vortices occurs nearly instantaneously once $H(t)$ exceeds H_s. It is the penetration of vortices which preserves the superconducting state at $H(t) > H_s$, as illustrated in figure 13. At $H < H_s$ the Meissner state is metastable, but at $H(t) > H_s$ the screening current density $J(0)$ at the surface exceeds J_c so to prevent the breakdown of superconductivity, vortices penetrate and produce a current counterflow which keeps $J(0)$ below J_c. Here, a delay with penetration of vortices at $\nu\tau_v \ll 1$ and $H > H_s$ would destroy superconductivity, but not extend the field region of the Meissner state. Measurements on Pb, In, InBi and SnIn at 90–300 MHz gave a breakdown field $H_b(T) \approx H_s(T)$ [201]. Pulse rf measurements on Nb gave $H_b(T) \approx H_s(T)$ at all T [204, 205]. However, for Nb_3Sn, it was found that $H_b(T) \approx H_s(T)$ only near T_c but becomes smaller than $H_s(T)$ at $T \ll T_c$ [204, 205].

The breakdown of the Meissner state at the static superheating field H_s at $\nu\tau_v \ll 1$ implies that nonequilibrium quasiparticles, for which the electron–phonon relaxation time $\tau_\epsilon(T)$ can exceed the rf period at $T \ll T_c$, do not play a significant role. This may happen in a dirty superconductor in which the quasiparticle gap ϵ_g remains finite at $H_a = H_s$ (see figure 8(c)). Here, the density of thermally-activated quasiparticles $n_{qp} \propto \exp(-\epsilon_g/k_B T)$ at $H_a = H_s$ and $k_B T \ll \epsilon_g$ is much smaller than the superfluid density n_s, so their slow relaxation has a negligible effect on the breakdown of superconducting condensate and $H_d \to H_s$. However, in a clean superconductor with $l_i > 8.7\xi_0$ the gap ϵ_g closes at $H_a < H_s$ so the breakdown

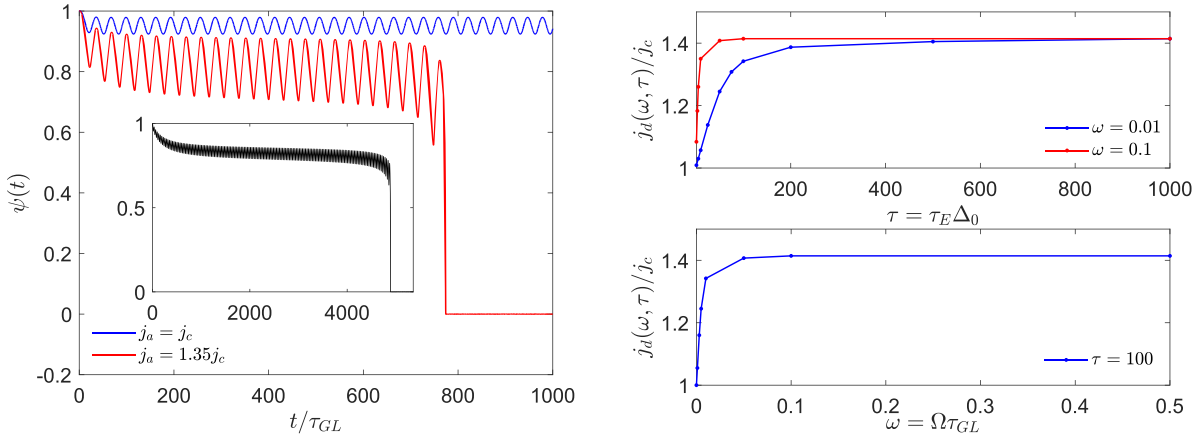

Figure 14. Left: time dependence of $\psi(t) = \Delta(t)/\Delta_0$ calculated at $J = J_a \sin\omega t$, $\hbar\omega = 0.1\Delta_0$, $\tau = \tau_E\Delta_0/\hbar = 10$, $J_a = J_c$ and the dynamic depairing current $J_d = 1.35J_c$ at which $\psi(t)$ vanishes abruptly. The inset shows $\psi(t)$ calculated at $\tau = 100$ and $J_a = \sqrt{2}J_c$. Right: dependencies of $J_d(\omega,\tau)$ on τ and ω. Here, J_d levels off at $\sqrt{2}J_c$ at $\Omega\tau_E \gg 1$, where Ω is the rf frequency. Reprinted figure with permission from [185], Copyright (2020) by the American Physical Society.

of superconductivity is affected by slow relaxation of quasiparticles with $n_{qp}(B_s) \sim n_s$, and the dynamic superheating field H_d can be different from H_s.

Calculation of a dynamic superheating field $H_d(T,\omega)$ or a dynamic depairing current density $J_d(T,\omega)$ requires solving equations of nonequilibrium superconductivity which account for the effects of rf current pairbreaking on the DOS and $\Delta(t)$ and the energy relaxation due to inelastic scattering of quasiparticles on phonons [83]. In the case of slow temporal and spatial variations of the order parameter $\psi(\mathbf{r},t) = \Delta(\mathbf{r},t)e^{i\chi(\mathbf{r},t)}$ and $\mathbf{J}(\mathbf{r},t)$ at $T \approx T_c$, these equations can be reduced to the time-dependent Ginzburg–Landau (TDGL) equations for a dirty gapped superconductor [83, 143]:

$$\frac{\tau_{\rm GL}}{\sqrt{1+(2\tau_\epsilon\Delta/\hbar)^2}}\left(\frac{\partial}{\partial t} + 2ie\varphi + \frac{2\tau_\epsilon^2}{\hbar^2}\frac{\partial\Delta^2}{\partial t}\right)\psi = \left(1-\frac{\Delta^2}{\Delta_0^2}\right)\psi + \xi_s^2(\nabla - 2ie\mathbf{A})^2\psi, \quad (36)$$

$$\mathbf{J} = -\frac{\pi\sigma_s}{4e\hbar k_{\rm B}T_c}\Delta^2(\nabla\chi + 2e\mathbf{A}) - \sigma_s\left(\nabla\varphi + \frac{\partial\mathbf{A}}{\partial t}\right), \quad (37)$$

Here $\xi_s = [\pi\hbar D_s/8k_{\rm B}(T_c - T)]^{1/2}$, $\tau_{\rm GL} = \pi\hbar/8k_{\rm B}(T_c - T)$, $\varphi(\mathbf{r},t)$ is the electric potential, $\Delta_0^2 = 8\pi^2k_{\rm B}^2T_c(T_c - T)/7\zeta(3)$, and $\sigma_s = 2e^2D_sN_s$. Equations (36) and (37) were derived from the kinetic BCS theory, assuming that $\mathbf{A}(\mathbf{r},t)$ and $\Delta(\mathbf{r},t)$ vary slowly over $\xi_s(0)$, the diffusion length $L_\epsilon = (D_s\tau_\epsilon)^{1/2}$ and τ_ε [83, 143].

The dynamic depairing current density $J_d(T,\omega)$ was calculated in [185] by solving both the TDGL equations and a full set of nonequilibrium equations for a dirty superconductor at $T \approx T_c$ [143]. Both approaches give qualitatively similar results, as illustrated in figure 14. The left panel of figure 14 shows how J_d is defined: the simulations start from an initial superconducting state until the steady state oscillations of $\Delta(t)$ set in at $J_a < J_d$. Once J_a is increased to J_d, $\Delta(t)$ drops to zero after a transient period. The dependencies of $J_d(\omega,\tau_\epsilon)$ on ω and the electron–phonon relaxation time τ_ε are shown in the right panels. One can see that $J_d(\omega)$ increases with ω and levels off at $J_d(\omega) \to \sqrt{2}J_c$ at $\omega\tau_\epsilon \gg 1$, which can be understood as follows.

Near T_c, the relaxation time constant $\tilde{\tau} = \tau_{\rm GL}\sqrt{1+(2\Delta_0\tau_\epsilon/\hbar)^2}$ of $\Delta(t)$ in equation (36) depends on both the GL time $\tau_{\rm GL}$ and the electron–phonon time τ_ε. At high frequencies, $\omega\tilde{\tau} \gg 1$, the order parameter cannot follow rapid oscillations of the magnetic drive $A(t)$ so $\Delta(t)$ undergoes small-amplitude temporal oscillations around a mean value $\bar{\Delta}$, as one can see in figure 14. Here $\bar{\Delta}$ is determined by equation (36) in which the pairbreaking term $4e^2A^2(t) \propto J_a^2\sin^2\omega t$ is replaced with its value $\langle J_a^2\sin^2\omega t\rangle = J_a^2/2$ averaged over the rf period. As a result, the pairbreaking term at $\omega\tilde{\tau} \gg 1$ is reduced by half as compared to low frequencies $\omega\tilde{\tau} \ll 1$ at which $\Delta(t)$ follows $J(t)$ adiabatically and the superconductivity breakdown occurs once the peak value of $J(t)$ exceeds J_c. Thus, the dynamic depairing current density J_d at $\omega\tilde{\tau} \gg 1$ is a factor $\sqrt{2}$ larger than the static J_c. The resulting enhancement of $H_d \to \sqrt{2}H_s$ at $\omega\tilde{\tau} \gg 1$ was obtained in [185] by solving both the TDGL equations and a full set of dynamic equations for $\Delta(t)$ and the kinetic equation for the nonequilibrium distribution function derived in [143]. In the dirty limit at $\kappa \gg 1$ the dynamic superheating field is related to J_d by $H_d = J_d\lambda$, where the field dependence of λ due to the nonlinear Meissner effect can be neglected. Calculations of $H_d(T,\omega,l_i)$ at a finite κ, particular in the clean limit at low temperatures, have not yet been done.

6. Surface nanostructuring

There is a strong interest in the development of superconducting resonant structures, with the breakdown magnetic field H_b exceeding the current state-of-the-art for Nb cavities [16, 17]. This task requires superconductors with H_s and T_c larger than H_s^{Nb} and T_c^{Nb} to provide lower R_s and higher breakdown fields in the Meissner state. Many such materials exist [47, 49], but all of them have H_{c1} lower than H_{c1}^{Nb}, which makes them more vulnerable to penetration of vortices and high rf losses at $H_a >$

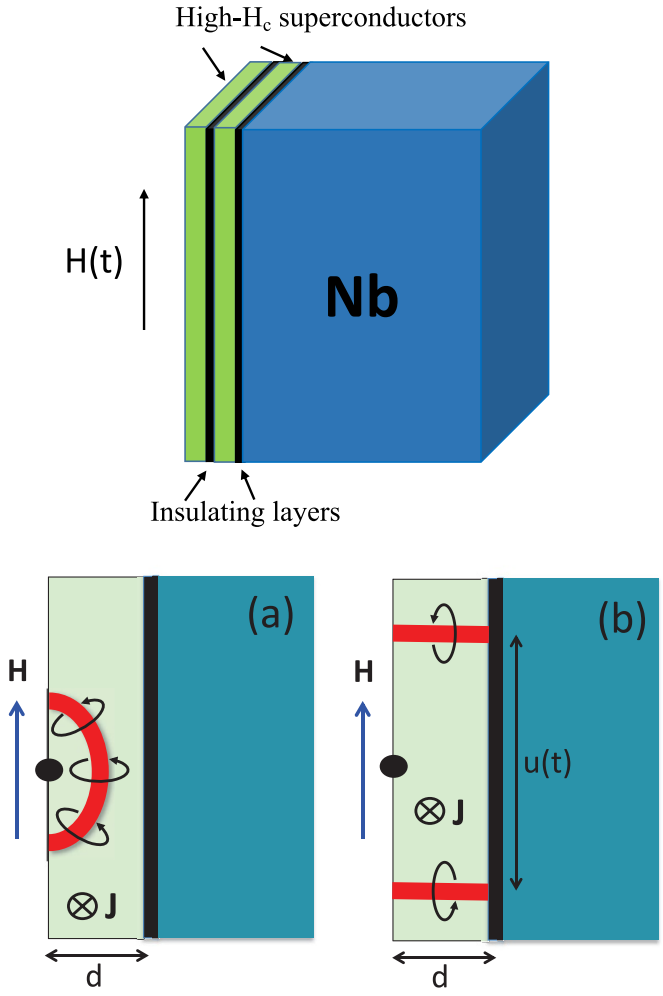

Figure 15. Top: SIS multilayer coating of a Nb substrate. Bottom: propagating vortex loop (a) turning into the vortex-antivortex pair (b) in the S layer with a surface defect (black dot) which lowers the field threshold of vortex penetration. Meissner current flows perpendicular to the screen. Reproduced from [44]. © IOP Publishing Ltd. All rights reserved.

H_{c1}. To address the low-H_{c1} problem of high-H_c materials, it has been proposed to coat the surface of Nb resonators with multilayers of thin superconductors (S) separated by dielectric (I) layers [43]. Here, the S layer material has H_s higher than the superheating field H_{s0} of Nb, whereas the thickness of S layers d is smaller than λ of the coating material and the thickness of I layers can be a few nm to suppress the Josephson coupling between S layers, as shown in figure 15. Such SIS structures can withstand rf fields limited by a higher superheating field of the S-layer: for instance, using Nb_3Sn with $B_c = 530$ mT [49] could potentially double the breakdown field as compared to Nb. In turn, the field onset of penetration of a parallel vortex in the S layer with $d \ll \lambda$ is increased because of a larger parallel $H_{c1} = (2\phi_0/\pi\mu_0 d^2)[\ln(d/\xi) - 0.07]$ in thin films [206, 207]. Here, H_{c1} at $d \ll \lambda$ depends weakly on the material properties, so getting $B_{c1} > 200$ mT requires $d_s < 100$ nm at $\xi_s = 5$ nm. Geometrical enhancement of H_{c1} has been observed on films of different materials in uniform parallel fields [208–214].

The maximum field H_m screened by the S layers of total thickness $d_s \gg \lambda$ is limited by the superheating field of the S coating material [43], for example, $B_s \simeq 0.84B_c = 454$ mT for Nb_3Sn at $T \ll T_c$. At $H = H_s$ the Meissner current in the top S layer becomes unstable and the magnetic barrier for penetration of vortices vanishes [22–25]. However, there is an optimum layer thickness d_m at which H_m exceeds the superheating fields of both the S-layer and the Nb substrate, as has been shown by numerical simulations of a parallel vortex in the London model [215–217], numerical simulations of the GL equations [217], and by analytical calculations of the depairing instability of Meissner currents [218]. The latter approach yields:

$$d_m = \lambda \ln\left(\mu + \sqrt{\mu^2 + k}\right), \tag{38}$$

$$H_m = \left[H_s^2 + \left(1 - \frac{\lambda_0^2}{\lambda^2}\right) H_{s0}^2\right]^{1/2}, \tag{39}$$

where $\mu = H_s\lambda/(\lambda + \lambda_0)H_{s0}$, and $k = (\lambda - \lambda_0)/(\lambda + \lambda_0) > 0$, and the subscript 0 labels the substrate properties. The optimum thickness is due to a counterflow induced by the substrate in the S-layer which can withstand higher fields if $\lambda > \lambda_0$ [44, 215, 218].

As follows from equations (38) and (39), H_m can also be enhanced by alloying the surface, where λ is increased due to a shorter mean free path [218]. For instance, a dirty Nb layer with $l_i \simeq 2$ nm has $\lambda \simeq \lambda_0(\xi_0/l_i)^{1/2} \simeq 180$ nm and $\xi = (l_i\xi_0)^{1/2} \simeq 9$ nm. Taking $B_s \approx 0.84B_c$ for $\kappa = \lambda_0/l_i = 20$ in equations (38) and (39), yields $d_m = 0.44\lambda = 79$ nm and $B_m = \mu_0 H_m = 1.44B_c = 288$ mT, some 20% higher than $B_{s0} = 240$ mT of pure Nb. If $\lambda_0^2 \ll \lambda^2$, equation (39) gives $B_m = \sqrt{B_s^2 + B_{s0}^2} = 1.465B_c = 293$ mT. Therefore, the maximum screening fields can be increased by depositing thin alloyed Nb layers at the surface of clean Nb, which may also bring the benefits of the field-induced reduction of $R_s(B_a)$. Evidence of enhanced vortex penetration field by a dirty Nb/Al_2O_3 bilayer deposited onto the Nb cavity was observed in [219].

Equations (38) and (39), obtained from the London theory are in good agreement with self-consistent numerical calculations of $H_s(d)$ from coupled Usadel and Maxwell equations for dirty SIS multilayers [159]. Shown in figure 16 are examples of $H_s(d)$ as functions of the overlayer thickness d calculated in [159] for dirty Nb, Nb_3Sn, NbN, and NbTiN deposited on the Nb substrate. Here, $H_s(d)$ first increases with d_s due to the counterflow effect [215, 218], reaches a cusp-like maximum and then decreases down to the superheating field of the S overlayer at $d \gg \lambda$. For cases a, c and d, the multilayers do not give a significant gain in the superheating field relative to $H_{s0} \approx 1.2H_{c0}$ at $\kappa \approx 1$ [24, 25] for the clean Nb. This reflects the fact that the layer materials shown in figure 16 except for Nb_3Sn have H_c not much higher than H_{c0} of Nb, and the calculations of [159] were done in the diffusive limit $l_i < \xi_0$ and $\kappa \gg 1$ in which $H_{s0} \simeq 0.8H_{c0}$ is about 35% smaller than H_{s0} at $\kappa \approx 1$. However, Nb_3Sn represented by figure 16(b) provides a significant gain in $H_m \approx 2.25H_{c0}$ relative to Nb, consistent with the proposal of [43].

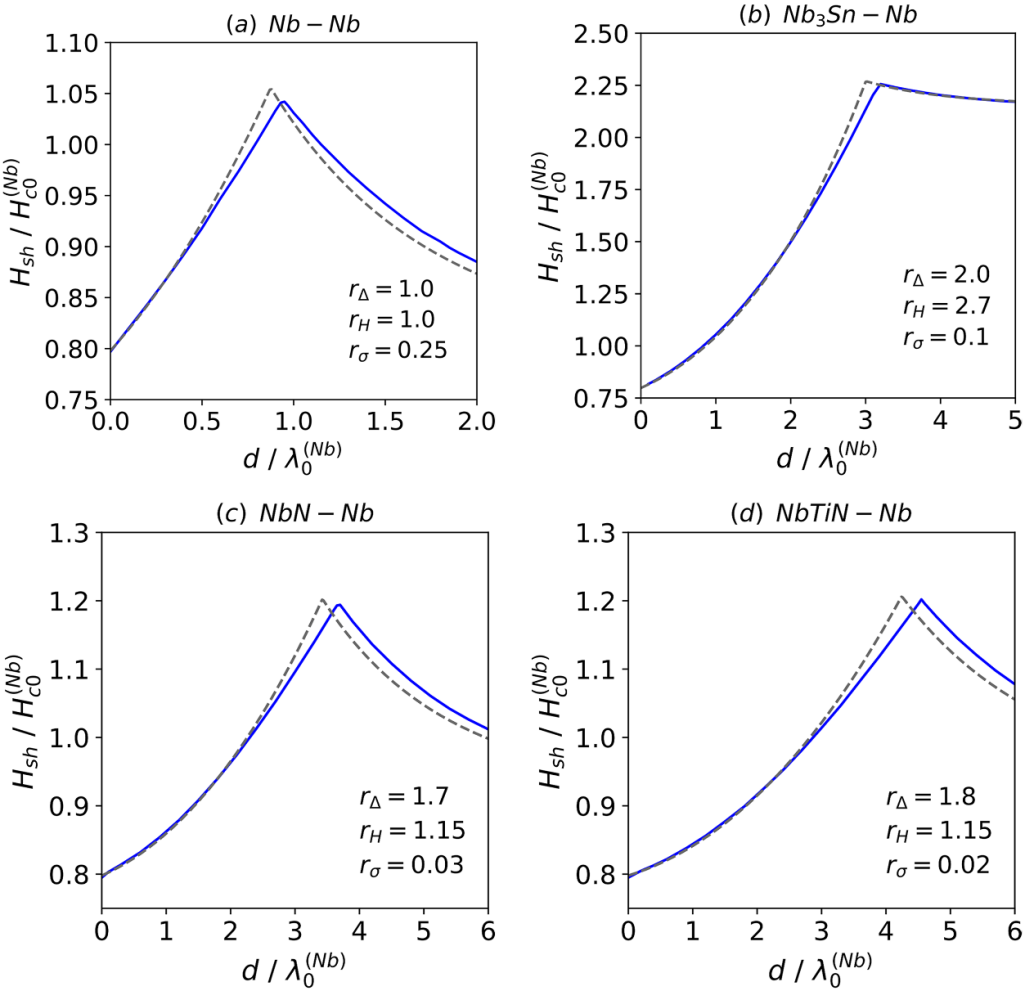

Figure 16. dc superheating fields as functions of the overlayer thickness d for Nb coated with different coating materials in the dirty limit and $\kappa \gg 1$. The solid curves are calculated by solving the coupled Maxwell–Usadel equations at $T \to 0$. The dashed curves show the London approximation in which the peak values d_m and H_m are given by equations (38) and (39): (a) dirty Nb–Nb structure with $(r_\Delta, r_H, r_\sigma) = (1, 1, 0.25)$. (b) Nb_3Sn–Nb structure with $(r_\Delta, r_H, r_\sigma) = (2, 2.7, 0.1)$. (c) NbN–Nb structure wiih $(r_\Delta, r_H, r_\sigma) = (1.7, 1.15, 0.03)$. (d) NbTiN-Nb structure with $(r_\Delta, r_H, r_\sigma) = (1.8, 1.15, 0.02)$. Here $r_\Delta = \Delta^i(0)/\Delta_0(0)$, $r_H = H_c^i(0)/H_{c0}(0)$, $r_\sigma = \sigma_s^i/\sigma_{s0}$, where $\Delta^i(0)$, $H_c^i(0)$, σ_s^i are the respective parameters of the ith coating material at $T = 0$, and the index 0 labels the parameters of Nb. Reproduced from [159].

Besides the deposition of a dirty film on the surface of a cleaner superconductor, H_m can also be increased by forming a dirty layer with a gradually decreasing concentration of nonmagnetic impurities as was shown in [220] by solving the Usadel equations with an inhomogeneous diffusivity $D(z) = D_\infty + D_1 \exp(-z/L_i)$, where L_i is the thickness of the dirty layer. Yet increasing H_m by producing a smooth profile of impurity concentration or direct deposition of an alloyed or a high-B_c layer onto a non-ideal S surface without a dielectric interlayer [216] does not necessarily widen the field region of the Meissner state. In the absence of I layer penetration of vortices at $H = H_m$ is impeded by the force $\mathbf{F} = -\nabla\varepsilon(x)$ caused by the gradient of the vortex energy $\varepsilon(x) = \phi_0^2 \ln\kappa(x)/4\pi\mu_0\lambda^2(x)$. For a smooth concentration profile, the maximum pinning force $F_p \sim \phi_0(H_{c10} - H_{c1})/L_i$ is much smaller than the pinning force $F_m \simeq H_{c10}/\xi_0$ for the S-I interface if $L_i \gg \xi$ and $\kappa \gg 1$. For a high-H_c or alloyed layer deposited directly onto Nb, the idealized sharp energy barrier due to a stepwise change in $\lambda(x)$ and $\xi(x)$ in the London model [216, 221] is, in fact, weakened by the proximity effect and inter diffusion of atomic components during film deposition at high temperatures, which broaden the vortex entry energy barrier and significantly reduce the pinning force.

In a SIS multilayer, the I layers assure the necessary stability margin with respect to proliferation of vortex semi-loops penetrating at surface defects. If these expanding vortex semi-loops are not stopped, they trigger thermomagnetic flux jumps [222–228], particularly at $T \ll T_c$, where the specific heat is small. At $H_{c1} < H_a < H_s$ the Meissner state remains metastable due to the Bean-Livingstron barrier [22]. Many magneto-optical imaging investigations of type-II superconductors [229–232] have revealed premature local penetration of vortices at grain boundaries and other materials and topographic defects at the surface [54–57]. In turn, TDGL and nonlinear electrodynamic simulations have shown that surface defects can reduce the penetration field [233–235]

and cause flux jets [236, 237] being precursors of themomagnetic avalanches.

Materials and topographic defects at the surface [7, 8, 238] reduce the local penetration field from H_s to a lower value H_i which can be close to H_{c1}. Figure 15 illustrates how the multilayer not only increases H_s but also blocks proliferation of vortices: a vortex semi-loop penetrating at a small defect in the first S layer cannot propagate further into the next S layer and then into the superconducting substrate where it can trigger a thermomagnetic avalanche. As $H(t)$ reaches H_i at a weak spot, the vortex semi-loop expands under the Lorentz force of the Meissner current until it hits the I layer, where most of the dissipative vortex core disappears in a loss-free flux channel connecting two short vortices of opposite polarity. This vortex-antivortex pair expands during the positive rf cycle and contracts and annihilates as $H(t)$ changes sign. The disappearance of most of the dissipative vortex core in the I interlayer does not happen in the case of direct deposition of a dirty or high-H_c layer onto the S substrate. Thus, the SIS multilayer reduces the vortex dissipation as compared to a thick Nb_3Sn film with $d \gg \lambda$ [44]. TDGL simulations of penetration of straight vortices into a SIS multilayer have been performed in [235].

Confinement of the rf power in a thin S layer inhibits expansion of multiple vortex loops in the bulk and blocks dendritic thermomagnetic avalanches that are particularly pronounced in Nb_3Sn, NbN or pnictides which have low σ_s and the thermal conductivity k [222, 239]. Yet, a thin Nb_3Sn layer with $d \sim 100$ nm only slightly increases the thermal impedance of the cavity wall, $G = \alpha_K^{-1} + d/k_s + d_i/k_i + d_{Nb}/k_{Nb}$, where α_K is the Kapitza interface thermal conductance. For $d_{Nb} = 3$ mm, $k_{Nb} \simeq 20$ W mK^{-1}, $\alpha_K = 2$ kW (m^{2}K)$^{-1}$, the Nb_3Sn multilayer with $d = 100$ nm, $k_s \simeq 10^{-2}$ W mK^{-1}, and Al_2O_3 dielectric layers with $d_i = 4$ nm and $k_i = 0.3$ W mK^{-1} increases G by $\simeq 5\%$ [9]. A thicker Nb_3Sn film with $d \simeq 2$–$3\,\mu$m doubles G and reduces the field of thermal quench, in addition to the smaller B_{c1} of bulk Nb_3Sn with $\lambda > 65$ nm [51] as compared to $B_{c1}^{Nb} \simeq 170$–180 mT.

Experiments on MgB_2, Nb_3Sn, NbN, NbTiN and dirty Nb as overlayers have shown an increase of the dc field onset of penetration of vortices on Nb surfaces coated with different SIS structures [208–214, 240–243]. However, the Q factors of SIS multilayers under high-amplitude rf fields $H_a \sim H_c$ have not yet been measured. Low-field measurements of Q on NbN/MgO multilayers [242] have shown that they can have lower R_s than bulk Nb. Recently Nb_3Sn/Al_2O_3 multilayers have been developed with a low-field R_s on par with R_s^{Nb} at $T > 4$ K [243]. The challenge with the measurements of $R_s(B_a)$ at high fields on materials with $H_c > H_c^{Nb}$ is the lack of experimental techniques capable of applying a strong parallel rf field $H_a \sim H_c$ to a thin film or a multilayer without dissipative penetration of vortices. Recently, Hall probe setups to measure a dc penetration field which quantifies the field onset of strong vortex dissipation in high-H_c film coatings were developed [239, 244]. The local nonlinear response of the Nb surface has been probed with a near-field magnetic microwave microscope [245]. Yet the quadrupole resonator [246] is currently the only available technique to measure the nonlinear surface resistance of large (7–8 cm in diameter) thin film multilayers at GHz frequencies.

7. Trapped vortices

Vortices are detrimental to high-Q structures in which even a small number of trapped vortices can dominate rf losses at $T \ll T_c$. Vortices can be trapped by material defects during the cooldown of a superconductor through T_c in a stray magnetic field. The field onset of penetration of perpendicular vortices in thin films $H_{c1}^{\perp} = (1 - N)H_{c1}$ is greatly reduced by the demagnetizing factor $N \to 1$ [74, 75]. Trapped vortices can limit Q at $T \ll T_c$ in thin film quantum circuits operating at mK temperatures [71–73] or resonant Nb cavities at $T < 1.5$ K and can give false signals in the search for magnetic monopoles [247]. Trapped magnetic flux can contribute to rf losses in different ways. In polycrystals with weakly coupled grain boundaries or granular films, Josephson vortices can penetrate along a network of weak links and give rise to losses at rf field amplitude H_a much smaller than H_{c1} [248–251]. Vortices can also be generated by thermoelectric currents in the case of direct deposition of a higher T_c film on top of a lower T_c substrate or in Nb coatings of Cu cavities. Here, temperature gradients arising upon cooling the sample produce magnetic flux when the temperature is reduced below the higher T_c of a bimetallic structure [252, 253]. This mechanism is suppressed in SIS multilayers in which I interlayers effectively decouple superconducting films with different T_c. Rf losses in cavities made of thin film type-I superconductors such as Al, result from trapped flux in the intermediate state [254].

The rest of this review focuses on rf losses of Abrikosov vortices with normal cores [18]. Such vortices trapped by a random pinning potential of material defects can bundle together, forming localized hotspots, which have been revealed by temperature mapping of Nb cavities [28, 79, 80] and thin film structures [81, 82], as well as by magnetic mapping [255–257]. Unlike hotspots caused by lossy material defects, vortex hotspots can be moved or fragmented by temperature gradients produced by external heaters [116] or scanning laser [80, 117, 258, 259] or electron [260, 261] beams. Low-field rf losses of pinned vortices have been thoroughly investigated in the literature [74, 80, 262–266]. The nonlinear quasi-static electromagnetic response of vortices has been evaluated qualitatively for both strong pinning [265, 267] and weak collective pinning [268]. Yet, the rf response of a perpendicular vortex in a film has distinctive features evident from figure 17 which shows examples of a vortex trapped by randomly distributed material defects in the bulk (a), pinning centers segregated at the surface (b) and clusters of pins (c). Here sparse vortices in high-Q resonators are driven by the Lorentz force of the surface Meissner current, which causes their bending distortions to extend over an elastic skin depth $L_\omega > \lambda$ [80]. As a result, a vibrating vortex segment interacts with only a few pins, while the rest of the vortex does not move. In this case, the rf response of the vortex becomes dependent on its

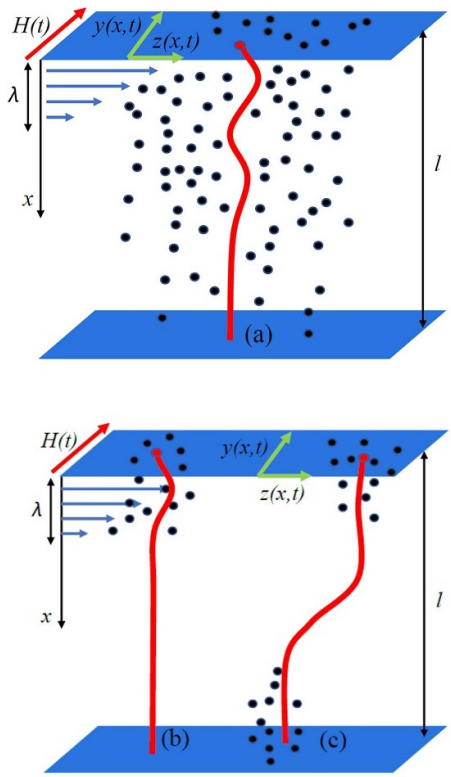

Figure 17. A trapped vortex driven by the rf surface current for different distributions of pinning centers shown by black dots: (a) bulk collective pinning (b) surface pinning (c) cluster pinning. Reprinted figure with permission from [270], Copyright (2021) by the American Physical Society.

position in a particular configuration of pinning centers, resulting in strong mesoscopic fluctuations of local R_i. Except for short vortices in thin films, the widely used Gittleman and Rosenblum model [262] is not applicable to the cases shown in figure 17 which require numerical simulations of a vibrating elastic vortex interacting with a few pinning centers [269–272].

The vortex trapped in a film is driven by the Meissner current density $J(0) \sim H/\lambda$ which can be much higher than the depinning current density J_p. For Nb at $B_a = 0.1B_c \simeq 20$ mT, we have $J(0) \sim 0.1J_d \sim 8 \times 10^{11}$ A m^{-2}, some 2–3 orders of magnitude higher than typical depinning J_p [265]. In this case, the tip of the vortex moves with a large velocity v mainly determined by the balance of the Lorentz force $F_L = \phi_0 J$ and the viscous drag force, $F_d = \eta(v)v$, where the vortex drag coefficient η can depend on v. Here $v \simeq \phi_0 J/\eta(v)$ can exceed the pairbreaking superfluid velocity of the condensate $v_c = \Delta/p_F$ at $J < J_c$ [20], where $v_c \simeq 1$ km s^{-1} for Nb. Vortices moving faster than the terminal velocity of the superflow which drives them have been observed on Pb and Nb–C films in which v can exceed v_c by 1–2 orders of magnitude [202, 203]. Such high velocities may result from the Larkin–Ovchinnikov (LO) mechanism in which $\eta(v)$ decreases with v as the moving vortex core becomes depleted of nonequilibrium quasiparticles lagging behind [273]. The LO theory predicts a nonmonotonic velocity dependence of the drag force $F_d = \eta(v)v$ which cannot balance the Lorentz force if v exceeds a critical value v_0. The LO instability has been observed by dc transport measurements on many superconductors [274–279] with typical values of $v_0 \sim 0.1$–1 km s^{-1} near T_c. At low T, the LO instability is masked by heating effects which are reduced if sparse trapped vortices are driven by the Meissner rf current. The velocity-dependent $\eta(v)$ and instability of the flux flow can also result from overheating of moving vortices [266, 270, 280, 281] or stretching of the vortex core along the direction of motion revealed by the TDGL simulations [202, 282, 283].

Addressing the variety of the observed field dependencies of $R_i(B_a)$ associated with trapped vortices [62–70] requires numerical simulations of a driven elastic curvilinear vortex in the case of mesoscopic pinning and a velocity-dependent $\eta(v)$. This was done in [270–272], where the vortex losses for pinning configurations shown in figure 17 were calculated by solving the dynamic equation for the coordinates $\mathbf{u} = [u_x(x,t), u_z(x,t)]$ of the vortex moving in the yz plane:

$$M\frac{\partial^2 \mathbf{u}}{\partial t^2} + \eta(v)\frac{\partial \mathbf{u}}{\partial t} = \varepsilon\frac{\partial^2 \mathbf{u}}{\partial x^2} - \nabla U(x,\mathbf{u}) + \hat{y}\frac{\phi_0 H_a}{\lambda}e^{-x/\lambda}\sin\omega t, \tag{40}$$

where M is the vortex mass per unit length and $\varepsilon = \phi_0^2(\ln\kappa + 0.5)/4\pi\mu_0\lambda^2$ is the vortex line energy at $\kappa \gg 1$ [74, 284]. Equation (40) represents a balance of local forces acting on a curvilinear vortex: the inertial and drag forces in the left hand side are balanced by the elastic, pinning and Lorentz forces in the right hand side. For the most efficient core pinning [74, 265, 284], $U(x,\mathbf{u})$ can be represented by a sum of pinning centers modeled by the Lorentzian potential wells of width of the core radius $\approx\xi$ [270, 285]:

$$U(x,\mathbf{u}) = -\sum_{n=1}^{N}\frac{U_n}{1 + [(x-x_n)^2 + |\mathbf{u} - \mathbf{r}_n|^2]/\xi^2}. \tag{41}$$

Here $x_n, \mathbf{r}_n = (y_n, z_n)$ are the coordinates of the nth pinning center and U_n is determined by the gain in the condensation energy of the vortex core at the pin [74, 265, 284]. The amplitude U_n defines the elementary pinning energy $u_p = \pi\xi U_n$ and the dimensionless pinning parameter $\zeta_n = 2\kappa^2 u_p/\pi\varepsilon\xi$. For a dielectric precipitate of radius $r_0 < \xi$, we have $u_p \sim B_c^2 r_0^3/\mu_0$ and $\zeta_n \sim (r_0/\xi)^3\kappa^2$ [265]. For a single impurity with a scattering cross-section σ_i, we have $u_p \sim B_c^2\sigma_i\xi/\mu_0$ [286] and $\zeta_n \sim \sigma_i\kappa^2/\xi^2$. In both cases ζ_n can be larger than 1 if $\kappa \gg 1$.

The viscous drag coefficient $\eta(v)$ can depend on v at high vortex velocities. For instance, the LO model gives [273]:

$$\eta = \frac{\eta_0}{1 + v^2/v_0^2}, \tag{42}$$

$$v_0^2 = \frac{D\sqrt{14\zeta(3)}}{\pi\tau_\epsilon(T)}\left(1 - \frac{T}{T_c}\right)^{1/2}. \tag{43}$$

Here $\eta_0 = \phi_0^2/2\pi\xi^2\rho_s$ is the Bardeen–Stephen drag coefficient [18], D is the electron diffusivity, and the quasiparticle energy relaxation time τ_ε is given by equation (29). A similar dependence of $\eta(v)$ on v can also result from overheating of a moving

vortex [266, 270, 280, 281]. The LO model predicts a non-monotonic velocity dependence of the drag force $F_d = \eta(v)v$ which can balance the Lorentz force $F_L = \phi_0 J$ only if $v < v_0$ and $F_L < \eta_0 v_0/2$. Jumps in the voltage-current characteristics caused by the LO instability have been observed in many superconductors [274–279] with $v_0 \sim 0.1$–$1\,\mathrm{km\,s^{-1}}$ near T_c. These experiments have shown that as T decreases, $v_0(T)$ first increases near T_c and then decreases at lower temperatures [278], consistent with equations (29) and (43). No direct measurements of $v_0(T)$ at low temperatures $T \ll T_c$ have been made.

The vortex mass $M_s \simeq 2p_F/\hbar\pi^3$ in equation (40) results from quasiparticles trapped in the vortex core [287], but other mechanisms producing $M \gg M_s$ have been suggested [288–290]. For instance, $M \sim 10^2 M_s$ was observed in Nb near T_c [291]. At GHz frequencies, the effect of the vortex mass on the overdamped vortex dynamics is negligible but becomes essential if the LO instability occurs. Another key characteristic of the vortex, shown in figure 17, is a complex penetration length L_ω of bending distortions induced by the surface rf Meissner current [44, 80]:

$$L_\omega = \sqrt{\frac{\varepsilon}{k_L + i\eta\omega}}, \tag{44}$$

where $k_L \sim \phi_0 J_p/\xi$ is the Labusch pinning spring constant [265]. At $\omega\eta \ll k_L$ equation (44) reduces to the Campbell penetration depth [265] or the Larkin pinning length $L_c \sim \xi\,(J_d/J_c)^{1/2}$ in the collective pinning theory [284]. At $\omega\eta \gg k_L$ equation (44) yields the elastic skin depth $L_\omega \to (\varepsilon/\eta\omega)^{1/2}$. For Nb_3Sn, $L_\omega \simeq 5.15\lambda = 572$ nm at 1 GHz, and $L_\omega \simeq 52\lambda = 5.7\,\mu$m at 10 MHz so the rf bending distortions of the vortex can extend well beyond the field penetration depth.

The nonlinear dynamics and rf dissipation of a trapped vortex was addressed by numerical simulations of two coupled nonlinear partial differential equations (40) for both $u_z(x,t)$ and $u_y(x,t)$ [270, 271]. In [269] the equation for u_z was disregarded. The power of rf losses $P = R_i H_a^2/2$ per unit area from all trapped vortices is expressed in terms of the residual resistance,

$$R_i = \frac{\rho_n B_0}{\lambda B_{c2}} r_i. \tag{45}$$

Here the dc inductance B_0 defines a mean areal density of trapped vortices $n_v = B_0/\phi_0$, and the dimensionless surface resistance $r_i = 2p(\beta,\gamma)/\beta^2$ is proportional to the normalized power $p = P/P_0$ per vortex which depends on the reduced rf field amplitude $\beta = B_a/B_{c1}$ and frequency $\gamma = \omega/\omega_0$, where

$$P_0 = \frac{\lambda\omega_0\varepsilon}{2\pi}, \qquad \omega_0 = \frac{2\pi B_{c1}\rho_n}{B_{c2}\lambda^2\mu_0}. \tag{46}$$

These definitions of γ and β adopted from [270, 271] should not be confused with the parameters β and γ used in the previous sections.

7.1. Weak rf fields

At weak rf fields, the vortex velocities are small $v \ll v_0$, so $\eta = \eta_0$ is independent of v and the effect of vortex mass at GHz frequencies is negligible. As shown in figure 18, the dimensionless surface resistance r_i calculated in [270] for pinning centers is distributed randomly over the film thickness (see figure 17(a)). The global surface resistance $\bar{r}$ obtained by averaging $r_i(\beta,k)$ for different random pin configurations with the same volume pin density is shown in figure 18(b). The vortex moving in a particular kth pinning landscape produces a unique $r_i(\beta,k)$ which can vary rather non-systematically with the rf field, reflecting many metastable positions of the curvilinear vortex in a random pinning potential. Figure 18(b) shows the result of averaging over ten different random pin distributions with the same $n_i = 1.67\lambda^{-3}$. The low-field $r_i(\beta,k)$ fluctuate strongly but converge to the same value at high fields. Here $r_i(\beta,k)$ at low fields is strongly affected by pinning, whereas $r_i(\beta,k)$ at higher fields is mostly limited by the vortex drag and the effect of mesoscopic pinning fluctuations weakens. The averaged $\bar{r}_i(\beta)$ shown in figure 18(b) first increases with β and levels off at $\beta > 0.2$ as the low-field $\bar{r}_i(\beta)$, which mostly results from pinning hysteretic losses, crosses over to a drag-dominated $\bar{r}_i(\beta)$. A similar low-field dependence of $R_i(H)$ has been observed in Nb cavities [268, 269].

7.2. Microwave reduction of $R_i(B_a)$ at high fields

The LO decrease of $\eta(v)$ with v can radically change the nonlinear dynamics of a trapped vortex and $R_i(B_a)$ at high fields and frequencies [270, 271]. Taking the LO effect into account raises the following questions: 1. What happens if the tip of the vortex moves faster than v_0 while the rest of the vortex does not? 2. How is the LO instability affected by pinning? 3. How does the decrease of $\eta(v)$ with v manifest itself in the dependencies of R_i on B_a, ω and the pinning strength? For a vortex segment pinned by a single strong pin, these issues were addressed in [271], and the effect of artificial pinning centers in films under a dc magnetic field and transport current was investigated in [292, 293]. The effect of LO instability is quantified by the control parameter α (not to be confused with α given by equation (23)) [270, 271]:

$$\alpha = (\lambda\omega/2\pi\, v_0)^2. \tag{47}$$

For $v_0 = 0.1$–$1\ \mathrm{km\,s^{-1}}$, equation (47) yields $\alpha = 4 \times (1$–$10^{-2})$ at $\lambda = 100$ nm and 2 GHz. The increase of α with ω indicates that manifestations of the LO mechanism become more pronounced at higher frequencies.

Shown in figure 19 is $r_i(\beta)$ calculated for random bulk pinning in a film of thickness $l = 10\lambda$ at $\zeta_n = 0.8$, $n_i = 0.25\lambda^{-3}$, and different values of α [270]. At the lowest frequency $\gamma = 0.01$ and $\alpha = 1$, the elastic skin depth $L_\omega = \lambda/\sqrt{2\pi\gamma} \approx 4\lambda$ is about half of the vortex length. In this case, the surface resistance decreases with the rf field due to the LO decrease of the vortex viscosity with v. A similar descending field dependence of $R_i(B_a)$ caused by the LO effect was obtained for a vortex pinned by a single defect [271], the results being independent

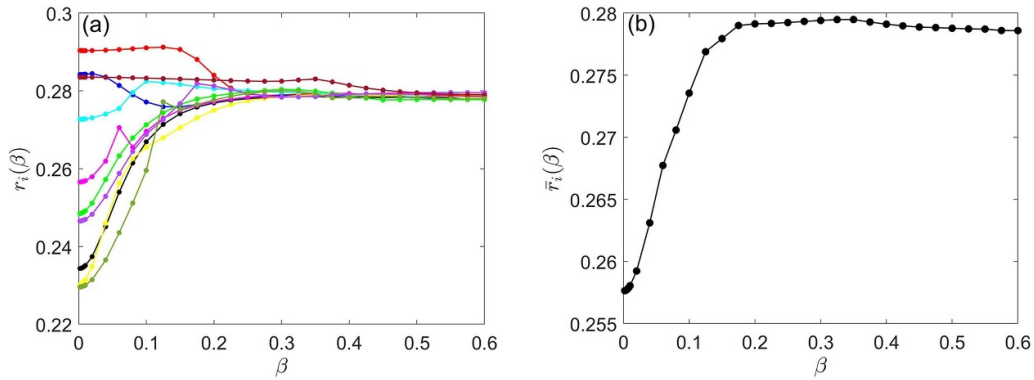

Figure 18. The dimensionless surface resistance $r_i(\beta)$ as a function of the normalized field $\beta = B_a/B_{c1}$ in a film of thickness at $d = 10\lambda$, $\nu = 0.04$, the pin density $n_i = 1.67\lambda^{-3}$, $\kappa = 10$ and $\zeta_n = 1$: (a) ten different random distribution of pins with the same density; (b) averaged $\bar{r}_i(\beta)$. Reprinted figure with permission from [270], Copyright (2021) by the American Physical Society.

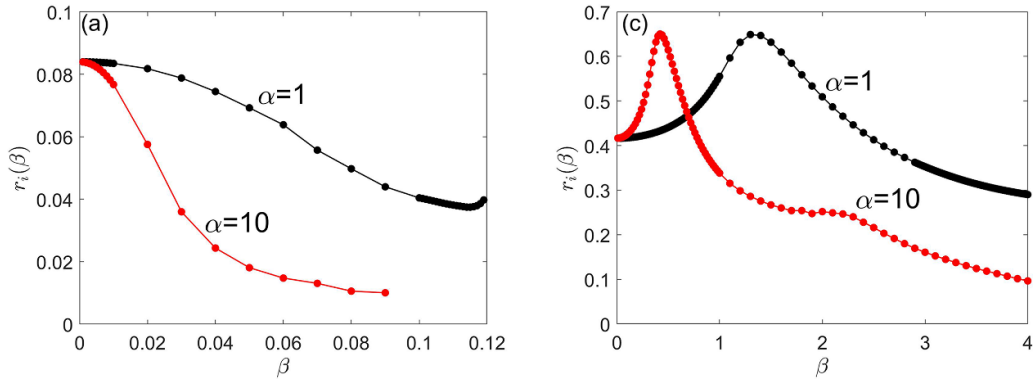

Figure 19. $r_i(\beta)$ as a function of $\beta = B_a/B_{c1}$ calculated for a film of thickness $l = 10\lambda$, $\kappa = 2$ in the case of bulk pinning with $\zeta_n = 0.8$, $n_i = 0.25\lambda^{-3}$, $\alpha = 1, 10$ and: (a) $\gamma = 0.01$, (c) $\gamma_0 = 1$. Reprinted figure with permission from [270], Copyright (2021) by the American Physical Society.

of the elementary pinning force if the pin is spaced more than L_ω from the surface.

At higher frequencies, the behavior of $r_i(\beta)$ changes, as shown in figure 19(c). Here $r_i(\beta)$ becomes nonmonotonic, the peaks in $r_i(\beta)$ shifting to lower fields as the LO parameter α increases. At the peak of $r_i(\beta)$ at $\beta = \beta_m$, the maximum velocity of the vortex tip v_m becomes of the order of v_0, but no LO vortex jumps occur because of the restoring effect of the vortex line tension. The increase of $r_i(\beta)$ with β at $\beta < \beta_m$ is mostly due to the increase of $L_\omega \sim [\epsilon/\eta(v)\omega]^{1/2}$ caused by the decreasing $\eta(v)$. At $\beta > \beta_m$ the elastic skin depth L_ω becomes of the order of the vortex length and $r_i(\beta)$ decreases with β due to the decrease of $\eta(v)$ with v [270, 271]. The peak velocity v_m of the vortex tip increases with B_a and can significantly exceed v_0 at high fields.

As β exceeds β_m, the dynamics of the vortex tip change from nearly harmonic oscillations at $\beta < \beta_m$ to highly anharmonic relaxation-type oscillations at $\beta > \beta_m$, the amplitude of oscillations increases greatly at $\beta > \beta_m$ [270]. Bending distortions along the vortex are mostly confined within the elastic skin depth L_ω which increases with v due to LO reduction of $\eta(v)$ and eventually becomes larger than l at $v_m > v_0$. The nonlinear dynamics of the vortex at $\beta > \beta_m$ becomes dependent on the vortex mass, the peaks in $r_i(\beta)$ shifting to higher β as the ω increases [270, 271].

The LO velocity dependence of $\eta(v)$ can produce the residual surface resistance which decreases with the rf field amplitude. Such field-induced reduction of $R_i(B_a)$ results from the interplay of vortex elasticity and the LO decrease of the viscous drag with the vortex velocity. The decrease of $R_i(B_a)$ with B_a can contribute to the negative $Q(B_a)$ slopes observed on alloyed Nb cavities [33–41]. Unlike the decrease of $R_i^{\rm TLS}(B_a)$ or the quasiparticle surface resistance with the rf field, the vortex contribution to $R_i(B_a)$ scales with the density of trapped magnetic flux. The field-induced reduction of $R_i(B_a)$ produced by trapped vortices becomes more pronounced at higher frequencies, which appears to be consistent with the experiment [39] on N-doped Nb cavities. As was shown in [271], the LO mechanism can account for $R_s(B_a) \propto B_a^{-2}$ observed on Nb cavities [28] which cannot be explained by the weaker field dependence of $R_i^{\rm TLS}(B_a)$.

7.3. *Tuning R_i by impurities*

The significance of vortex losses in high-Q resonators brings to focus approaches for decreasing R_i by material treatments.

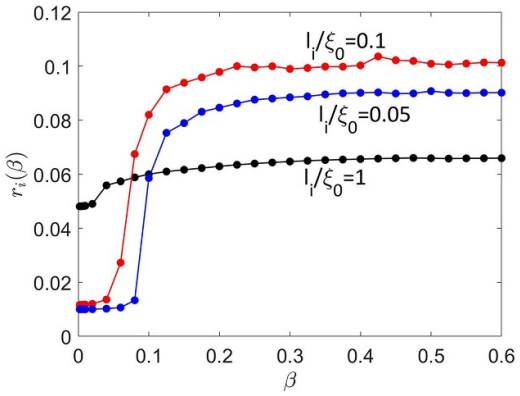

Figure 20. Field dependence of $r_i(\beta)$ on $\beta = B_a/B_{c10}$ for a film of thickness $l = 10\lambda_0$ at $\kappa_0 = 2$, $\zeta_{n0} = 0.04$, $\gamma_0 = 0.004$, $n_i = 0.5\lambda_0^{-3}$ and different mean free paths. Reproduced from [272].

The vortex losses at low fields can be reduced by increasing the volume density and strength of pinning centers. Consider first a reduction of R_i by alloying a superconductor with nonmagnetic impurities without changing the pinning defect structure. This was addressed in [270–272] by incorporating the dependencies of $\lambda = g\lambda_0$, $\xi = \xi_0/g$, and the pinning parameter $\zeta_n = 2\kappa^2 u_p/\pi\varepsilon\xi = \zeta_{n0}g^5$ on the mean free path l_i into equations (40) and (41). Here, the conventional factor $g = (1+\xi_0/l_i)^{1/2}$ interpolates the dependencies of superconducting properties on the mean free path [18], ζ_n is evaluated for small dielectric inclusions for which $u_p \sim B_c^2 r_0^3/\mu_0$ is independent of l_i, and the index 0 labels the parameters of a clean material. The vortex viscosity η and the LO parameter α at $l_i < \xi_0$ can be evaluated as $\eta \simeq \eta_0 g^2 l_i/\xi_0$ and $\alpha \simeq \alpha_0 g^2 \xi_0/l_i$ using equation (43) with $D = l_i v_F/3$ and τ_ε being independent of l_i (see also [294]). Hence, alloying the material with $l_i < \xi_0$ results in the following:

- Enhances the pinning parameter $\zeta_n \sim \zeta_{n0}(\xi_0/l_i)^{5/2}$ as the vortex core diameter $\xi \sim (l_i\xi_0)^{1/2}$ and the line tension $\varepsilon \sim \varepsilon_0 l_i/\xi_0$ decrease. This increases the elementary pinning forces and allows a softer vortex to better accommodate the pins.
- Weakly affects the Bardeen–Stephen vortex drag coefficient η_0 which becomes independent of l_i at $l_i \ll \xi_0$.
- Facilitates manifestations of the velocity dependence of $\eta(v)$ in the residual resistance $R_i(B_a)$ as the LO parameter $\alpha \sim \alpha_0(\xi_0/l_i)^2$ increases.

The field dependence of $r_i(B_a)$ calculated in [272] for bulk pinning in a film with different mean free paths and the Bardeen–Stephen η_0 is shown in figure 20. The overall behavior of $r_i(B_a)$ is similar to that shown in figure 18(b): the dip in $r_i(B_a)$ at low field occurs if the sheet Meissner current B_a is smaller than the rf depinning field $B_p \sim \mu_0 J_p L_\omega$. At $B_a < B_p$ the vortex undergoes small-amplitude oscillations impeded by pinning which reduces rf losses. At $B_a > B_p$ the surface resistance increases significantly as the net Lorentz force exceeds the pinning force, and the amplitude of vortex oscillations is primarily determined by the balance of Lorentz and viscous drag forces. The transition from the pinning-dominated to viscous drag dominated regimes shifts to higher fields as pinning becomes more effective upon alloying the material. Yet alloying increases $r_i(B_a)$ at higher fields, although r_i drops a bit as l_i is decreased from $0.1\xi_0$ to $0.05\xi_0$. The latter reflects a nonmonotonic dependence of R_i of a freely moving vortex segment on l_i: $R_i \propto l_i^{-1/2}$ at $L_\omega > \lambda$ and $R_i \propto l_i^{1/2}$ at $L_\omega < \lambda$ [80].

Figure 21 shows the effect of the mean free path on the microwave reduction of $R_i(B_a)$ caused by the LO velocity dependence of $\eta(v)$ for a vortex pinned by a single defect spaced by $l = 3\lambda_0$ from the surface [271]. One can see that the decrease of $R_i(B_a)$ with B_a becomes stronger and shifts to lower fields upon alloying the material. This reflects the increase of the LO control parameter $\alpha \propto (\omega\xi_0/l_i)^2$ as ω increases and l_i decreases. A maximum in $R_i(B_a)$ in figure 21 appears at high frequencies at which L_ω becomes smaller than l, similar to the evolution of $R_i(B_a,\omega)$ shown in figure 19. The descending dependence of $R_i(B_a)$ at high fields can be masked by overheating [270].

7.4. Pinning optimization

Low-field rf losses of trapped vortices can be reduced by making pinning more effective using designer pinning structures which have been very effective in increasing J_p in superconductors for dc magnets [295, 296]. However, the artificial pinning centers in high-Q resonators can only be used in the form of dielectric precipitates or nano pores because metallic pins (for example, α-Ti ribbons in NbTi [295]) can produce high rf losses. Consider an upper limit of J_p for strong pinning by small dielectric precipitates or pores of radius $r_0 \simeq \xi$ which chop vortex lines into short segments of length $\ell < \lambda$. If the ends of each vortex segment are fixed by the strong pins, J_p is determined by the pin breaking mechanism [297, 298] in which vortices bow out under the action of the Lorentz force and escape as the tips of two antiparallel vortex segments at the pin reconnect at the critical current density $J_p \sim \varepsilon/\phi_0\ell$ which increases with the pin density $n_p = \ell^{-3}$ [74]. However, too many dielectric pins would block the current-carrying cross section so $J_p(\ell)$ is determined by the interplay of pinning and current blocking [298]:

$$J_p \simeq \frac{\phi_0}{2\pi\mu_0\lambda^2\ell}\ln\frac{\ell}{2\xi}\left(1-\frac{4\pi r_0^3}{3p_c\ell^3}\right). \qquad (48)$$

Here the factor in the parenthesis accounts for the reduction of the current-carrying cross section by dielectric pins and p_c is the percolation threshold which varies from $p_c = 1/2$ in two dimensions to $p_c \simeq 2/3$ in the 3D isotropic limit [300]. The interplay of pinning and current blocking yields a maximum of $J_p(\ell)$ at $\ell_m \simeq (16\pi/3p_c)^{1/3} r_0 \simeq 3r_0$, an optimal volume fraction of pins $p_m \simeq 9\%$–12% and the maximum $J_{pm} \simeq (0.2$–$0.3)J_d$, where the spread of numerical values comes from the shapes of pins and the effect of crystalline anisotropy [298]. The maximum in J_p at $p \sim 10\%$ was also revealed by TDGL numerical simulations of vortices interacting with

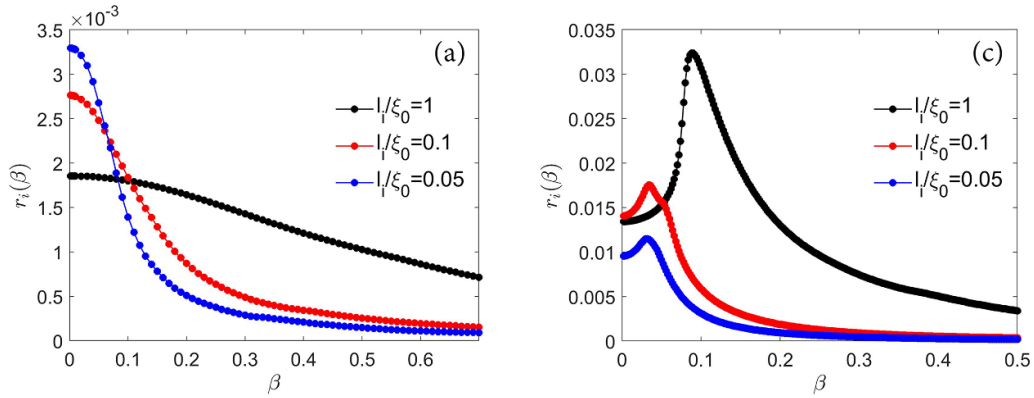

Figure 21. The surface resistance $r_i(\beta)$ calculated for a vortex pinned by a strong pin located at $l = 3\lambda_0$ for different values of l_i/ξ_0: (a) $\gamma_0 = 0.004$, $\alpha_0 = 0.1$, (c) $\gamma_0 = 0.4$, $\alpha_0 = 1000$. Reprinted figure with permission from [271], Copyright (2020) by the American Physical Society.

metallic pinning centers [299]. The optimized pinning with $J_p \simeq 0.2J_d$ allows a superconductor with sparse trapped vortices to withstand without significant losses the applied rf field $B_m \simeq \mu_0 J_{pm}\lambda \simeq 0.2B_c$. Yet, even such idealized pinning structures can only provide rf breakdown fields much smaller than $B_b \simeq B_c$ observed on Nb cavities [16, 17]. Thus, pinning can only reduce the residual surface resistance at $B_a \ll B_c$.

The reduction of R_i by increasing the volume fraction of dielectric pins can come at the expense of higher dielectric and quasiparticle rf losses because dielectric precipitates increase the composite magnetic penetration depth $\bar{\lambda}$. This follows from the effective medium theory [301] which gives the conductivity $\bar{\sigma} = (1 - p/p_c)\sigma$ [300, 301] of a composite comprised of dielectric spherical precipitates of radius r_0 and the volume fraction $p = 4\pi r_0^3/3\ell^3$ embedded in a matrix with conductivity σ. At $T \ll T_c$, we have $\sigma_1 \ll \sigma_2$ so $\sigma \to i\sigma_2 = i/\mu_0\omega\lambda^2$ and $\bar{\sigma} = (1 - p/p_c)\sigma = i/\mu_0\omega\bar{\lambda}^2$. Hence, $\bar{\lambda}(p)$ increases with p and diverges at the percolation threshold $p = p_c$:

$$\bar{\lambda} = \frac{\lambda}{\sqrt{1 - p/p_c}}. \tag{49}$$

According to equations (2) and (49), the surface resistance $\bar{R}_{\rm BCS} \propto \bar{\lambda}^3$ increases with p. For a small fraction of dielectric pins $p \ll p_c$, we have $\bar{\lambda} = \lambda(1 + 3p/4)$ and

$$\bar{R}_{\rm BCS} = \left(1 + 3\pi r_0^3/\ell^3\right) R_{\rm BCS}. \tag{50}$$

At the optimum pin spacing $\ell \simeq 3r_0$ the composite surface resistance $\bar{R}_{\rm BCS}$ is increased by about 30% relative to $R_{\rm BCS}$. Vortex trapping depends strongly on the sample geometry and is most pronounced in thin films in which the perpendicular B_{c1} is greatly reduced. Vortex losses in thin film coplanar resonators were eliminated by producing an array of microscopic pinholes of radius $r_0 > \xi$ which fully absorb the dissipative vortex and block vortex motion [71–73]. Such columnar pins result in a very high depinning current density $J_p \sim J_c$ [302, 303]. At the same time, the pinholes can increase the TLS losses at the edges [73].

8. Conclusions and outlook

Decreasing microwave losses in high-Q superconducting structures involves dealing with interconnected mechanisms, tuning one of them to increase Q can cause others to decrease Q. For example, reducing the residual surface resistance which controls the limits of Q at ultra low temperatures requires minimizing the broadening of the DOS peaks and TLS losses. By contrast, reducing $R_{\rm BCS}(T)$ at intermediate temperatures requires engineering an optimum DOS broadening by tuning the concentration of magnetic impurities or properties of a proximity coupled metallic suboxide at the surface. In turn, the proximity effect can be used to either significantly increase or decrease the kinetic inductance L_k of thin film resonators, although increasing L_k by using granular Al films would also increase TLS losses in oxide inter-grain contacts. Thus, a universal optimization of rf properties of superconductors is hardly possible as different applications operating in their respective ranges of temperatures, frequencies and rf fields require different superconducting materials and their treatments. For instance, accelerator cavities operating at 2 K mostly use Nb as the best compromise for the many conflicting requirements outlined above.

Reducing TLS losses is a challenging problem as the atomic origin and microscopic mechanisms of TLS are not fully understood, although O vacancies and O–H vacancy complexes in Nb and Al oxides seem to be viable candidates. TLS losses may be decreased by material treatments which reduce the density of excess O vacancies, make the oxide layer thinner and less amorphous and reduce segregation of O vacancies at grain boundaries [173–175]. In this regard, the mid-T baking of Nb cavities, which reduced the residual resistance below 1 nΩ [32], may offer a new path for optimization of Nb resonators in quantum circuits. Furthermore, TLS losses in thin film resonators in transmons operating at very low fields $H \ll H_c$ can be reduced by using type-I superconductors with less complex surface oxide structures than Al or Nb. For instance, the use of tantalum thin film resonators with $T_c \approx 4.3$ K and $B_c \approx 83$ mT [49] can increase the Q factor by 2–4 times as compared to Nb or Al resonators [304, 305].

The detrimental effect of trapped vortices can be mitigated by optimizing pinning to reduce vortex losses at $H_a \ll H_c$. The field region of the Meissner state can be extended by SIS multilayers which also reduce vortex losses, although the I interlayers may increase TLS losses. On the other hand, strong pinning increases the number of vortices trapped during the cooldown through T_c since it prevents vortices from escaping the film as the temperature decreases and $H_{c1}(T)$ becomes larger than H. Another way of reducing the losses of trapped vortices would be to get rid of them by better magnetic shielding combined with cooling the films in temperature gradients to push the maximum number of trapped vortices out by using scanning laser [80, 117, 258, 259] or electron [260, 261] beams before they get stuck on pinning centers.

In addition to their important applications, high-Q superconducting resonators can be used to probe the fundamental limits of dissipation and dynamic superheating fields in superconductors at low temperatures. These issues involve outstanding theoretical problems related to the mechanisms of subgap states and the nonlinear response of nonequilibrium superconductors in strong rf fields. Furthermore, high-Q resonators can be testbeds for probing extreme nonlinear dynamics of vortices driven by strong rf Meissner currents, particularly the terminal velocity and nonequilibrium processes in the rapidly moving vortex core, which are masked by heating to a much lesser extent than in dc transport experiments.

Data availability statement

No new data were created or analysed in this study.

Acknowledgment

This work was supported by DOE under Grant DE-SC 100387-020.

ORCID iD

Alex Gurevich https://orcid.org/0000-0003-0759-8941

References

[1] Blais A, Grimsmo A L, Girvin S M and Wallraff A 2021 *Rev. Mod. Phys.* **93** 025005
[2] Day P K, LeDuc H G, Mazin B A, Vayonakis A and Zmuidzinas J 2003 *Nature* **425** 817
[3] Natarajan C M, Tanner M G and Hadfield R H 2012 *Supercond. Sci. Technol.* **25** 063001
[4] Zadeh I E, Chang J, Los J W N, Gyger S, Elshaari A W, Steinhauer S, Dorenbos S N and Zwiller V 2021 *Appl. Phys. Lett.* **118** 190502
[5] Zmuidzinas J 2012 *Annu. Rev. Condens. Matter. Phys.* **3** 169
[6] Hofheinz M *et al* 2009 *Nature* **459** 546
[7] Padamsee H, Knobloch J and Hays T 2007 *RF Superconductivity for Accelerators* 2nd edn (New York: Wiley)
[8] Antoine C Z 2012 (DSM IRFU CEA Centre d'Etudes de Saclay) Materials and surface aspects in the development of SRF Niobium cavities *Report* EuCARD-BOO-2012-001
[9] Gurevich A 2012 *Rev. Accel. Sci. Technol.* **5** 119
[10] Mattis D C and Bardeen J 1958 *Phys. Rev.* **111** 412
[11] Nam S B 1967 *Phys. Rev.* **156** 487
[12] Turneaure J P, Halbritter J and Schwettman H A 1991 *J. Supercond.* **4** 341
[13] Turneaure J P and Weissman I 1968 *J. Appl. Phys.* **39** 4417
[14] Hein M A 2002 *Microwave Properties of Superconductors* (*NATO ASI Series* vol 375) pp 21–53
[15] Jackson J D 1989 *Classical Electrodynamics* 3rd edn (New York: Wiley)
[16] Geng R L 2006 *Physica* C **441** 145
[17] Geng R L, Eremeev G V, Padamsee H and Shemelin V D 2007 *Proc. PAC2007 (Albuquerque, NM, USA)* p 2337
[18] Tinkham M 1996 *Introduction to Superconductivity* (New York: Dover)
[19] Parmenter R H 1962 *RCA Rev.* **23** 323
[20] Bardeen J 1962 *Rev. Mod. Phys.* **34** 667
[21] Maki K 1969 *Superconductivity* vol 2, ed R D Parks (New York: Marcel Dekker Inc.) p 1035
[22] Bean C P and Livingston J D 1964 *Phys. Rev. Lett.* **12** 14
[23] Galaiko V P 1966 *Sov. Phys.—JETP* **23** 475
[24] Matricon J and Saint-James D 1967 *Phys. Lett.* A **24** 241
[25] Chapman S J 1995 *SIAM J. Appl. Math.* **55** 1233
[26] Catelani G and Sethna J P 2008 *Phys. Rev.* B **78** 224509
[27] Lin F P-J and Gurevich A 2012 *Phys. Rev.* B **85** 054513
[28] Ciovati G 2004 *J. Appl. Phys.* **96** 1591
[29] Visemtin V, Barthe M F, Moineau V and Desgardin P 2010 *Phys. Rev. ST Accel. Beams* **13** 052002
[30] Ciovati C, Myneni G, Stevie F, Maheshawari P and Griffis D 2010 *Phys. Rev. ST Accel. Beams* **13** 022002
[31] Trenikhina Y, Romanenko A, Kwon J, Zuo J-M and Zasadzinski J F 2015 *J. Appl. Phys.* **117** 154507
[32] Posen S, Romanenko A, Grassellino A, Melnychuk O S and Sergatskov D A 2020 *Phys. Rev. Appl.* **13** 014024
[33] Dhakal P *et al* 2013 *Phys. Rev. ST Accel. Beams* **16** 042001
[34] Grassellino A, Romanenko A, Sergatskov D, Melnychuk O, Trenikhina Y, Crawford A, Rowe A, Wong M, Khabiboulline T and Barkov F 2013 *Supercond. Sci. Technol.* **26** 102001
[35] Ciovati G, Dhakal P and Gurevich A 2014 *Appl. Phys. Lett.* **104** 092601
[36] Gonnella D *et al* 2015 *J. Appl. Phys.* **117** 023908
[37] Grassellino A *et al* 2017 *Supercond. Sci. Technol.* **30** 094004
[38] Ciovati G, Dhakal P and Myneni G R 2016 *Supercond. Sci. Technol.* **29** 064002
[39] Martinello M, Checchin M, Romanenko A, Grassellino A, Aderhold S, Chandrasekeran S, Melnychuk O, Posen S and Sergatskov D 2018 *Phys. Rev. Lett.* **121** 224801
[40] Lechner E M, Angle J W, Stevie F A, Kelley M J, Reece C E and Palczewski A D 2021 *Appl. Phys. Lett.* **119** 082601
[41] Dhakal P 2020 *Phys. Open* **5** 100034
[42] Posen S, Lee J, Seidman D N, Romanenko A, Tennis B, Melnychuk O S and Sergatskov D A 2021 *Supercond. Sci. Technol.* **34** 025007
[43] Gurevich A 2006 *Appl. Phys. Lett.* **88** 012511
[44] Gurevich A 2017 *Supercond. Sci. Technol.* **30** 034004
[45] Gurevich A and Kubo T 2017 *Phys. Rev.* B **96** 184515
[46] Kubo T and Gurevich A 2019 *Phys. Rev.* B **100** 064522
[47] Valente-Feliciano A-M 2016 *Supercond. Sci. Technol.* **29** 113002
[48] McConville T and Serin B 1965 *Phys. Rev.* **140** A1169
[49] Roberts B W 1976 *J. Phys. Chem. Ref. Data* **5** 581
[50] Perpeet M, Hein M A, Müller G, Piel H, Pouryamout J and Diete W 1997 *J. Appl. Phys.* **82** 5021
[51] Andreone A, Cassinese A, Di Chiara A, Iavarone M, Palomba F, Ruosi A and Vaglio R 1997 *J. Appl. Phys.* **82** 1736

[52] Deambrosis S M, Keppel G, Ramazzo V, Roncolato C, Sharma R G and Palmieri V 2006 *Physica* C **441** 108
[53] Cody G D and Cohen R W 1964 *Rev. Mod. Phys.* **36** 121
[54] Suenaga M and Jansen W 1983 *Appl. Phys. Lett.* **43** 791
[55] Sandim M J R, Tytko D, Kostka A, Choi P, Awaji S, Watanabe K and Raabe D 2013 *Supercond. Sci. Technol.* **26** 055008
[56] Lee J, Posen S, Mao Z, Trenikhina Y, He K, Hall D L, Liepe M and Seidman D N 2019 *Supercond. Sci. Technol.* **32** 024001
[57] Durrell J H, Eom C-B, Gurevich A, Hellstrom E E, Tarantini C, Yamamoto A and Larbalestier D C 2011 *Rep. Prog. Phys.* **74** 124511
[58] Dynes R C, Narayanamurti V and Garno J P 1978 *Phys. Rev. Lett.* **41** 1509
[59] Zasadzinski J 2004 *The Physics of Superconductors* vol 1, ed K H Bennemann and J B Ketterson (New York: Springer) pp 591–643
[60] Phillips W A 1987 *Rep. Prog. Phys.* **50** 1657
[61] Müller C, Cole J H and Lisenfeld J 2019 *Rep. Prog. Phys.* **82** 124501
[62] Vogt J M, Kugeler O and Knobloch J 2013 *Phys. Rev. ST Accel. Beams* **16** 102002
[63] Romanenko A, Grassellino A, Melnychuk O and Sergatskov D A 2014 *J. Appl. Phys.* **115** 184903
[64] Posen S, Checchin M, Crawford A C, Grassellino A, Martinello M, Melnychuk O S, Romanenko A, Sergatskov D A and Trenikhina Y 2016 *J. Appl. Phys.* **119** 213903
[65] Checchin M, Martinello M, Romanenko A, Grassellino A, Sergatskov D, Posen S, Melnychuk O and Zasadzinski J 2016 *Phys. Rev. Appl.* **5** 044019
[66] Huang S, Kubo T and Geng R L 2016 *Phys. Rev. Accel. Beams* **19** 082001
[67] Gonnella D, Kaufman J and Liepe M 2016 *J. Appl. Phys.* **119** 073904
[68] Checchin M, Martinello M, Grassellino A, Romanenko A and Zasadzinski J F 2017 *Supercond. Sci. Technol.* **30** 034003
[69] Kramer F, Kugeler O, Köszegi J-M and Knobloch J 2020 *Phys. Rev. Accel. Beams* **23** 123101
[70] Dhakal P, Ciovati G and Gurevich A 2020 *Phys. Rev. Accel. Beams* **23** 023102
[71] Song C, DeFeo M P, Yu K and Plourde B L T 2009 *Appl. Phys. Lett.* **95** 232501
[72] Bothner D *et al* 2012 *Appl. Phys. Lett.* **100** 012601
[73] Chiaro B *et al* 2016 *Supercond. Sci. Technol.* **29** 104006
[74] Brandt E H 1995 *Rep. Prog. Phys.* **58** 1456
[75] Prozorov R and Kogan V G 2018 *Phys. Rev. Appl.* **10** 014030
[76] Maniv A, Polturak E and Koren G 2003 *Phys. Rev. Lett.* **91** 197001
[77] Golubchik D, Polturak E, Koren G, Shapiro B Y and Shapiro I 2011 *J. Low Temp. Phys.* **164** 74
[78] Kirtley J R, Tsuei C C and Tafuri F 2003 *Phys. Rev. Lett.* **90** 257001
[79] Knobloch J, Muller H and Padamsee H 1994 *Rev. Sci. Instrum.* **65** 3521
[80] Gurevich A and Ciovati G 2013 *Phys. Rev.* B **87** 054502
[81] Song C, Heitmann T W, DeFeo M P, Yu K, McDermott R, Neeley M, Martinis J M and Plourde B L T 2009 *Phys. Rev.* B **79** 174512
[82] Kurter C, Zhuravel A P, Ustinov A V and Anlage S M 2011 *Phys. Rev.* B **84** 104515
[83] Kopnin N B 2001 *Theory of Nonequilibrium Superconductivity* (New York: Oxford University Press)
[84] Carbotte J P 1990 *Rev. Mod. Phys.* **62** 1027
[85] Blaschke R and Blocksdorf R 1982 *Z. Phys.* **9** 99–108
[86] Marsiglio F, Carbotte J P, Akis R, Achkir D and Poirier M 1994 *Phys. Rev.* B **50** 7204
[87] Mori T, Nicol E J, Shiizuka S, Kuniyasu K, Nojima T, Toyota N and Carbotte J P 2008 *Phys. Rev.* B **77** 174515
[88] Lee W, Rainer D and Zimmermann W 1989 *Physica* C **159** 535
[89] Zhou S, Jabbar A, Bao J-S, Wu K and Jin B 1992 *J. Appl. Phys.* **71** 2789
[90] Balatskii A V, Vekhter I and Zhu J-X 2006 *Rev. Mod. Phys.* **78** 373
[91] Proslier T, Zasadzinski J F, Cooley L, Antoine C, Moore J, Norem J, Pellin M and Gray K E 2008 *Appl. Phys. Lett.* **92** 212505
[92] Proslier T, Zasadzinski J, Cooley L, Pellin M, Norem J, Elam J, Antoine C Z, Rimmer R A and Kneisel P 2009 *IEEE Trans. Appl. Supercond.* **19** 1404
[93] Becker C, Posen S, Groll N, Cook R, Schlepütz C M, Hall D L, Liepe M, Pellin M, Zasadzinski J and Proslier T 2015 *Appl. Phys. Lett.* **106** 082602
[94] Skvortsov M A and Feigel'man M V 2013 *J. Exp. Theor. Phys.* **117** 487
[95] Devereaux T P and Belitz D 1991 *Phys. Rev.* B **44** 4587
[96] Browne D A, Levin K and Muttalib K A 1987 *Phys. Rev. Lett.* **58** 156
[97] Bennett A N 1965 *Phys. Rev.* **140** A1902
[98] Larkin A I and Ovchinnikov Y N 1972 *Sov. Phys.—JETP* **34** 1144
[99] Meyer J S and Simons B D 2001 *Phys. Rev.* B **64** 134516
[100] Wolf E L and Arnold G B 1982 *Phys. Rep.* **91** 31
[101] de Graaf S E, Faoro L, Ioffe L B, Mahashabde S, Burnett J J, Lindström T, Kubatkin S E, Danilov A V and Tzalenchuk A Y 2020 *Sci. Adv.* **6** 5055
[102] Kaplan S B, Chi C C, Langenberg D N, Chang J J, Jafarey S and Scalapino D J 1976 *Phys. Rev.* B **14** 4854
[103] Herman F and Hlubina R 2017 *Phys. Rev.* B **96** 014509
[104] Leyronas X and Combescot R 1996 *Phys. Rev.* B **54** 3482
[105] Bonin B and Safa H 1991 *Supercond. Sci. Technol.* **4** 257
[106] Attanasio C, Maritato L and Vaglio R 1991 *Phys. Rev.* B **43** 6128
[107] Andreone A, Cassinese A, Iavarone M, Vaglio R, Kulik I O and Palmieri V 1995 *Phys. Rev.* B **52** 4473
[108] Pappas D P, Vissers M R, Wisbey D S, Kline J S and Gao J 2011 *IEEE Trans. Appl. Supercond.* **21** 871
[109] Romanenko A and Schuster D I 2017 *Phys. Rev. Lett.* **119** 264801
[110] Isagawa S 1980 *J. Appl. Phys.* **51** 6010
[111] Trenikhina Y, Romanenko A, Kwon J, Zuo J-M and Zasadzinski J F 2015 *J. Appl. Phys.* **117** 154507
[112] Benvenuti C, Calatroni S, Campisi I E, Darriulat P, Peck M A, Russo R and Valente A-M 1999 *Physica* C **316** 153
[113] Benvenuti C, Calatroni S, Darriulat P, Peck M-A, Valente A-M and Van't Hof C A 2001 *Physica* C **351** 421
[114] Calatroni S 2006 *Physica* C **441** 95
[115] Birnbaum H K, Grossbecr M L and Amano M 1976 *J. Less-Common Met.* **49** 357
[116] Ciovati G and Gurevich A 2008 *Phys. Rev. ST Accel. Beams* **11** 122001
[117] Ciovati G *et al* 2012 *Rev. Sci. Instrum.* **83** 034704
[118] Fominov Y V, Houzet M and Glazman L I 2011 *Phys. Rev.* B **84** 224517
[119] Kharitonov M, Proslier T, Glatz A and Pellin M J 2012 *Phys. Rev.* B **86** 024514
[120] Groll N R, Becker C, Ciovati G, Grassellino A, Romanenko A, Zasadzinski J F and Proslier T 2019 arXiv:1805.06359v1
[121] Lechner E M, Dev Oli B, Makita J, Ciovati G, Gurevich A and Iavarone M 2020 *Phys. Rev. Appl.* **13** 044044
[122] Robertazzi R P, Kleinsasser A W, Laibowitz R B, Koch R H and Stawiasz K G 1992 *Phys. Rev.* B **46** 8456
[123] Ekin J W, Russek S E, Clickner C C and Jeanneret B 1993 *Appl. Phys. Lett.* **62** 369

[124] Tung R T 2015 *Appl. Phys. Rev.* **1** 011304
[125] Golubov A A and Kuprianov M Y 1989 *Sov. Phys.—JETP* **69** 805
[126] Belzig W, Bruder C and Schön G 1986 *Phys. Rev.* B **54** 9443
[127] Fulde P 1965 *Phys. Rev.* **137** A783
[128] Anthore A, Pothier H and Esteve D 2003 *Phys. Rev. Lett.* **90** 127001
[129] Oates D E 2007 *J. Supercond. Novel Magn.* **20** 3
[130] Sridhar S and Mercerau J E 1996 *Phys. Rev.* B **43** 203
[131] Hein M A, Oates D E, Hirst P J, Humphreys R G and Velichko A V 2002 *Appl. Phys. Lett.* **80** 1007
[132] de Visser P J, Goldie D J, Diener P, Withington S, Baselmans J J A and Klapwijk T M 2014 *Phys. Rev. Lett.* **112** 047004
[133] Pippard A B 1950 *Proc. R. Soc.* **203** 210
[134] Spiewak M 1959 *Phys. Rev.* **113** 1479
[135] Sharvin Y V and Gantmakher V F 1961 *Sov. Phys.—JETP* **12** 866
[136] Richards P L 1962 *Phys. Rev.* **126** 912
[137] Lewis R T 1964 *Phys. Rev.* **134** A1
[138] Glosser R 1967 *Phys. Rev.* **156** 500
[139] Koch J F and Kuo C C 1967 *Phys. Rev.* **164** 618
[140] Garfunkel M P 1968 *Phys. Rev.* **173** 516
[141] Larkin A I and Ovchinnikov Y N 1986 *Nonequilibrium Superconductivity* ed D N Langenberg and A I Larkin (Amsterdam: North Holland) p 493
[142] Belzig W, Wilhelm F K, Bruder C, Schön G and Zaikin A D 1999 *Superlattices Microstruct.* **25** 1251
[143] Watts-Tobin R J, Krähenbühl Y and Kramer L 1981 *J. Low Temp. Phys.* **42** 459
[144] Sauls J A 2022 *Prog. Theor. Exp. Phys.* **2022** 033I03
[145] Mooij J E 1981 *Nonequilibrium Superconductivity, Phonons and Kapitza Boundaries* ed K E Gray (New York: Plenum) p 191
[146] Dmitriev V M, Gubankov V N and Nad' F Y 1986 *Nonequilibrium Superconductivity* ed D N Langenberg and A I Larkin (Amsterdam: North Holland) p 163
[147] Semenov A V, Devyatov I A, de Visser P J and Klapwijk T M 2016 *Phys. Rev. Lett.* **117** 047002
[148] Eliashberg G M and Ivlev B I 1986 *Nonequilibrium Superconductivity* ed D N Langenberg and A I Larkin (Amsterdam: North-Holland) p 211
[149] Tikhonov K S, Semenov A V, Devyatov I A and Skvortsov M A 2020 *Ann. Phys., NY* **417** 168101
[150] Gurevich A 2014 *Phys. Rev. Lett.* **113** 087001
[151] Shurakov A, Lobanov Y and Goltsman G 2016 *Supercond. Sci. Technol.* **29** 023001
[152] Orlando T P, McNiff E J, Foner S and Beasley M R 1979 *Phys. Rev.* B **19** 4545
[153] Ashkroft N W and Mermin N D 1976 *Solid State Physics* (Philadelphia, PA: Holt, Rinehart and Winston)
[154] Leo A, Grimaldi G, Citro R, Nigro A, Pace S and Huebener R P 2011 *Phys. Rev.* B **84** 014536
[155] Zhang L *et al* 2018 *Sci. Rep.* **8** 1486
[156] Sidorova M *et al* 2020 *Phys. Rev.* B **102** 054501
[157] Kubo T 2020 *Phys. Rev. Res.* **2** 033203
[158] Kubo T 2020 *Phys. Rev. Res.* **2** 013302
[159] Kubo T 2021 *Supercond. Sci. Technol.* **34** 045006
[160] Kubo T 2022 *Phys. Rev. Appl.* **17** 014018
[161] Powers R W and Doyle M V 1959 *J. Appl. Phys.* **30** 514
[162] Hahn H and Halama H J 1976 *J. Appl. Phys.* **47** 4629
[163] Dacca A, Gemme G, Mattera L and Parodi R 1998 *Appl. Surf. Sci.* **126** 219
[164] Ma Q, Ryan P, Freeland J W and Rosenberg R A 2004 *J. Appl. Phys.* **96** 7675
[165] Delheusy M, Stierle A, Kasper N, Kurta R P, Vlad A, Dosch H, Antoine C, Resta A, Lundgren E and Andersen J 2008 *Appl. Phys. Lett.* **92** 101911
[166] Sebastian J T, Seidman D N, Yoon K E, Bauer P, Reid T, Boffo C and Norem J 2006 *Physica* C **441** 70
[167] Yoon K E, Seidman D N, Antoine C and Bauer P 2008 *Appl. Phys. Lett.* **93** 132502
[168] Tao R, Todorovic R, Liu J, Meyer R J, Arnold A, Walkosz W, Zapol P, Romanenko A, Cooley L D and Klie R F 2011 *J. Appl. Phys.* **110** 124313
[169] Fang X, Oh J-S, Kramer M, Romanenko A, Grassellino A, Zasadzinski J and Zhou L 2022 *Mater. Res. Lett.* **11** 108
[170] Burnett J, Faoro L and Lindström T 2016 *Supercond. Sci. Technol.* **29** 044008
[171] Altoé M V P *et al* 2022 *Phys. Rev. Quantum* **3** 020312
[172] Lisenfeld J, Bilmes A, Megrant A, Barends R, Kelly J, Klimov P, Weiss G, Martinis J M and Ustinov A V 2019 *npj Quantum Inf.* **5** 105
[173] Premkumar A *et al* 2021 *Commun. Mater.* **2** 72
[174] Murthy A A *et al* 2022 *ACS Nano* **16** 17257
[175] Wenskat M *et al* 2022 *Phys. Rev.* B **106** 094516
[176] Halama H J 1971 *Appl. Phys. Lett.* **19** 90
[177] Vissers M R, Gao J, Sandberg M, Duff S M, Wisbey D S, Irwin K D and Pappas D P 2013 *Appl. Phys. Lett.* **102** 232603
[178] Catalano A *et al* 2015 *Astron. Astrophys.* **580** A15
[179] Hu J, Salatino M, Traini A, Chaumont C, Boussaha F, Goupil C and Piat M 2020 *J. Low Temp. Phys.* **199** 355
[180] Cooper L N 1961 *Phys. Rev. Lett.* **6** 689
[181] Deutscher G and de Gennes P G 1969 *Superconductivity* vol 2, ed R D Parks (New York: Marcel Dekker, Inc.) p 1005
[182] Golubov A A, Kupriyanov M Y and Il'ichev E 2004 *Rev. Mod. Phys.* **76** 411
[183] Gurevich A 2018 *Phys. Rev.* B **98** 024506
[184] Semenov A V, Devyatov I A, Westig M P and Klapwijk T M 2020 *Phys. Rev. Appl.* **13** 024079
[185] Sheikhzada A and Gurevich A 2020 *Phys. Rev.* B **102** 104507
[186] Xu D, Yip S K and Sauls J A 1995 *Phys. Rev.* B **51** 16233
[187] Dahm T and Scalapino D J 1997 *J. Appl. Phys.* **81** 2002
[188] Li M-R, Hirschfeld P J and Wolfle P 2000 *Phys. Rev.* B **61** 648
[189] Zaikin A D 1982 *Solid State Commun.* **41** 533
[190] Belzig W, Bruder C and Schön G 1996 *Phys. Rev.* B **53** 5727
[191] Fauchère A L and Blatter G 1997 *Phys. Rev.* B **56** 14102
[192] Belzig W, Bruder C and Fauchère A L 1989 *Phys. Rev.* B **58** 14531
[193] Rotzinger H, Skacel S T, Pfirrmann M, Voss J N, Münzberg J, Probst S, Bushev P, Weides M P, Ustinov A V and Mooij J E 2017 *Supercond. Sci. Technol.* **30** 025002
[194] Maleeva N *et al* 2018 *Nat. Commun.* **9** 3889
[195] Winkel P *et al* 2020 *Phys. Rev.* X **10** 031032
[196] Makita J, Sundahl C, Ciovati G, Eom C B and Gurevich A 2022 *Phys. Rev. Res.* **4** 013156
[197] Barone A and Paterno G 1982 *Physics and Applications of Josephson Effect* (New York: Wiley)
[198] Brandt E H 2003 *Phys. Rev.* B **68** 054506
[199] Kupriyanov M Y and Likichev V F 1980 *Fiz. Niz. Temp.* **6** 445Kupriyanov M Y and Likichev V F 1980 *Sov. J. Low Temp. Phys.* **6** 210 (Engl. transl.)
[200] Nicole E J and Carbotte J P 1991 *Phys. Rev.* B **43** 10210
[201] Yogi T, Dick G J and Mercereau J E 1977 *Phys. Rev. Lett.* **39** 826
[202] Embon L *et al* 2017 *Nat. Commun.* **8** 85
[203] Dobrovolskiy O V, Vodolazov D Y, Porrati F, Sachser R, Bevz V M, Mikhailov M Y, Chumak A V and Huth M 2020 *Nat. Commun.* **11** 3291
[204] Posen S, Valles N and Liepe M 2015 *Phys. Rev. Lett.* **115** 047001
[205] Keckert S *et al* 2019 *Supercond. Sci. Technol.* **32** 075004
[206] Abrikosov A A 1964 *Sov. Phys.—JETP* **19** 988
[207] Stejic G, Gurevich A, Kadyrov E, Christen D, Joynt R and Larbalestier D C 1994 *Phys. Rev.* B **49** 1247

[208] Civale L, Worthington T K and Gupta A 1993 *Phys. Rev.* B **48** 7576
[209] Antoine C Z, Berry S, Bouat S, Jacquot J-F, Villegier J-C, Lamura G and Gurevich A 2010 *Phys. Rev. ST Accel. Beams* **13** 121001
[210] Tajima T *et al* 2012 *AIP Conf. Proc.* **1435** 297
[211] Antoine C Z, Villegier J-C and Martinet G 2013 *Appl. Phys. Lett.* **102** 102603
[212] Beringer D B, Clavero C, Tan T, Xi X X, Roach W M and Lukaszew R A 2013 *IEEE Trans. Appl. Supercond.* **23** 75006
[213] Roach W M, Beringer D B, Li Z, Clavero C and Lukaszew R A 2013 *IEEE Trans. Appl. Supercond.* **23** 86002
[214] Tan T, Wolak M A, Acharya N, Krick A, Lang A C, Sloppy J, Taheri M L, Civale L, Chen K and Xi X X 2015 *APL Mater.* **3** 041101
[215] Kubo T, Iwashita Y and Saeki T 2014 *Appl. Phys. Lett.* **104** 032603
[216] Kubo T 2017 *Supercond. Sci. Technol.* **30** 023001
[217] Liarte D B, Posen S, Transtrum M K, Catelani G, Liepe M and Sethna J P 2017 *Supercond. Sci. Technol.* **30** 033002
[218] Gurevich A 2015 *AIP Adv.* **5** 017112
[219] Russo R, Catani L, Cianchi A, DiGiovenale D, Lorkiewicz J, Tazzari S, Granata C, Ventrella P, Lamura G and Andreone A 2009 *IEEE Trans. Appl. Supercond.* **19** 1394
[220] Ngampruetikorn V and Sauls J A 2019 *Phys. Rev. Res.* **1** 012015
[221] Mkrtchyan G S and Shmidt V V 1975 *Sov. Phys.—JETP* **41** 90
[222] Mints R G and Rakhmanov A L 1981 *Rev. Mod. Phys.* **53** 551
[223] Aranson I, Gurevich A and Vinokur V 2001 *Phys. Rev. Lett.* **87** 0670031
[224] Altshuler E and Johansen T H 2004 *Rev. Mod. Phys.* **76** 471
[225] Aranson I S, Gurevich A, Welling M S, Wijngaarden R J, Vlasko-Vlasov V K, Vinokur V M and Welp U 2005 *Phys. Rev. Lett.* **94** 0370021
[226] Vestgarden J I, Shantsev D, Galperin Y M and Johansen T H 2011 *Phys. Rev.* B **84** 054537
[227] Mikheenko P, Qviller A J, Vestgarden J I, Chaudhuri S, Maasilta I J, Galperin Y M and Johansen T H 2013 *Appl. Phys. Lett.* **102** 022601
[228] Colauto F, Vestgarden J, de Andrade A M H, Oliveira A A M, Ortiz W A and Johansen T H 2013 *Appl. Phys. Lett.* **103** 032604
[229] Polyanskii A A, Cai X Y, Feldmann D M and Larbalestier D C 1999 *Nano-Crystalline and Thin Film Magnetic Oxides* (*NATO Science Series 3* vol 72) ed I Nedkov and M Ausloos (Amsterdam: Kluwer Academic Publishers) pp 353–70
[230] Jooss C, Albrecht J, Kuhn H, Leonhardt S and Kronmüller H 2002 *Rep. Prog. Phys.* **65** 651
[231] Ooi S, Tachiki M, Konomi T, Kubo T, Kikuchi A, Arisawa S, Ito H and Umemori K 2021 *Phys. Rev.* B **104** 064504
[232] Wang M, Polyanskii A, Balachandran S, Chetri S, Crimp M A, Lee P J and Bieler T R 2022 *Supercond. Sci. Technol.* **35** 045001
[233] Vodolazov D Y 2000 *Phys. Rev.* B **62** 8691
[234] Pack A R, Carlson J, Wadsworth S and Transtrum M K 2020 *Phys. Rev.* B **101** 144504
[235] Wang Q-Y, Xue C, Dong C C and Zhou Y-H 2022 *Supercond. Sci. Technol.* **35** 045004
[236] Friesen M and Gurevich A 2001 *Phys. Rev.* B **63** 064521
[237] Bezuglyj A I, Shklovskij V A, Budinská B, Aichner B, Bevz V M, Mikhailov M Y, Vodolazov D Y, Lang W and Dobrovolskiy O V 2022 *Phys. Rev.* B **105** 214507
[238] Ries R, Seiler E, Gömöry F, Medvids A, Onufrijevs P, Pira C, Chyhyrynets E, Malyshev O B and Valizadeh R 2022 *Supercond. Sci. Technol.* **35** 075010
[239] Senevirathne I H, Gurevich A and Delayen J R 2022 *Rev. Sci. Instrum.* **93** 055104
[240] Tan T, Wolak M A, Xi X X, Tajima T and Civale L 2016 *Sci. Rep.* **6** 35879
[241] Junginger T, Wasserman W and Laxdal R E 2017 *Supercond. Sci. Technol.* **30** 125012
[242] Antoine C Z, Aburas M, Four A, Weiss F, Iwashita Y, Hayano H, Kato S, Kubo T and Saeki T 2019 *Supercond. Sci. Technol.* **32** 085005
[243] Sundahl C, Makita J, Welander P B, Su Y-F, Kametani F, Xie L, Zhang H, Li L, Gurevich A and Eom C-B 2021 *Sci. Rep.* **11** 7770
[244] Turner D A, Malyshev O B, Burt G, Junginger T, Valizadeh R and Gurran L 2022 *Supercond. Sci. Technol.* **35** 095004
[245] Oripov B *et al* 2019 *Phys. Rev. Appl.* **11** 064030
[246] Keckert S, Kleindienst R, Kugeler O, Tikhonov D and Knobloch J 2021 *Rev. Sci. Instrum.* **92** 064710
[247] Groom D E 1986 *Phys. Rep.* **140** 323
[248] Hylton T L and Beasley M R 1989 *Phys. Rev.* B **39** 9042
[249] McDonald J and Clem J R 1997 *Phys. Rev.* B **56** 14723
[250] Gurevich A 2002 *Phys. Rev.* B **65** 214531
[251] Sheikhzada A and Gurevich A 2017 *Phys. Rev.* B **95** 214507
[252] Van Harlingen D J 1982 *Physica* B **109–110** 1710
[253] Shelly C D, Matrozova E A and Petrashov V T 2016 *Sci. Adv.* **2** e1501250
[254] Catelani G, Li K, Axline C J, Brecht T, Frunzio L, Schoelkopf R J and Glazman L I 2022 *Supercond. Sci. Technol.* **35** 065016
[255] Schmitz B, Köszegi J, Alomari K, Kugeler O and Knobloch J 2018 *Rev. Sci. Instrum.* **89** 054706
[256] Parajuli I P, Ciovati G and Delayen J R 2021 *Rev. Sci. Instrum.* **92** 104705
[257] Okada T, Kako E, Masuzawa M, Sakai H, Ueki R, Umemori K and Tajima T 2022 *Phys. Rev. Accel. Beams* **25** 082002
[258] Klein B E, Seo S, Kwon C, Park B H and Jia Q X 2022 *Rev. Sci. Instrum.* **73** 3692
[259] Zhuravel A P, Anlage S M, Remillard S K, Lukashenko A V and Ustinov A V 2010 *J. Appl. Phys.* **108** 033928
[260] Huebener R P 1984 *Rep. Prog. Phys.* **47** 175
[261] Gross R and Koelle D 1994 *Rep. Prog. Phys.* **57** 651
[262] Gittleman J I and Rosenblum B 1966 *Phys. Rev. Lett.* **16** 734
[263] Coffey M W and Clem J R 1992 *Phys. Rev.* B **45** 9872
[264] Golosovsky M, Tsindlekht M and Davidov D 1996 *Supercond. Sci. Technol.* **9** 1
[265] Campbell A M and Evetts J E 1972 *Adv. Phys.* **21** 199
[266] Gurevich A and Ciovati G 2008 *Phys. Rev.* B **77** 104501
[267] Willa R, Geshkenbein V B, Prozorov R and Blatter G 2015 *Phys. Rev. Lett.* **115** 207001
[268] Liarte D B, Hall D, Koufalis P N, Miyazaki A, Senanian A, Liepe M and Sethna J P 2018 *Phys. Rev. Appl.* **10** 054057
[269] Checchin M and Grassellino A 2020 *Phys. Rev. Appl.* **14** 044018
[270] Pathirana W P M R and Gurevich A 2021 *Phys. Rev.* B **103** 184518
[271] Pathirana W P M R and Gurevich A 2020 *Phys. Rev.* B **101** 064504
[272] Pathirana W P M R and Gurevich A 2021 *Proc. Int. Conf. RF Superconductivity (Michigan State University, Lansing, 28 June 2021)* p TU055
[273] Larkin A I and Ovchinnikov Y N 1975 *Sov. Phys.—JETP* **41** 960
[274] Musienko L E, Dmitrienko I M and Volotskaya V G 1980 *Sov. Phys.—JETP Lett.* **31** 567
[275] Klein W, Huebener R P, Gauss S and Parisi J 1985 *J. Low Temp. Phys.* **61** 413
[276] Villard C, Peroz C and Sulpice A 2003 *J. Low Temp. Phys.* **131** 957

[277] Armenio A A, Bell C, Aarts J and Attanasio C 2007 *Phys. Rev.* B **76** 054502
[278] Leo A, Grimaldi G, Citro R, Nigro A, Pace S and Huebener R P 2011 *Phys. Rev.* B **84** 014536
[279] Bezuglyj A I, Shklovskij V A, Vovk R V, Bevz V M, Huth M and Dobrovolskiy O V 2019 *Phys. Rev.* B **99** 174518
[280] Bezuglyj A I and Shklovskij V A 1992 *Physica* C **202** 234
[281] Kunchur M N 2002 *Phys. Rev. Lett.* **89** 137005
[282] Vodolazov D Y 2012 *Phys. Rev.* B **85** 174507
[283] Grimaldi G, Leo A, Sabatino P, Carapella G, Nigro A, Pace S, Moshchalkov V V and Silhanek A V 2015 *Phys. Rev.* B **92** 024513
[284] Blatter G, Feigel'man M V, Geshkenbein V B, Larkin A I and Vinokur V M 1994 *Rev. Mod. Phys.* **66** 1125
[285] Embon L *et al* 2015 *Sci. Rep.* **5** 7598
[286] Thuneberg E V, Kurkijärvi J and Rainer D 1984 *Phys. Rev.* B **29** 3913
[287] Suhl H 1965 *Phys. Rev. Lett.* **14** 226
[288] Kopnin N B and Vinokur V M 1998 *Phys. Rev. Lett.* **81** 3952
[289] Sonin E B, Geshkenbein V B, van Otterlo A and Blatter G 1998 *Phys. Rev.* B **57** 575
[290] Chudnovsky E M and Kuklov A B 2003 *Phys. Rev. Lett.* **91** 067004
[291] Golubchik D, Polturak E and Koren G 2012 *Phys. Rev.* B **85** 060504
[292] Grimaldi G, Leo A, Nigro A, Silhanek A V, Verellen N, Moshchalkov V V, Milošević M V, Casaburi A, Cristiano R and Pace S 2012 *Appl. Phys. Lett.* **100** 202601
[293] Silhanek A V *et al* 2012 *New J. Phys.* **14** 053006
[294] In [269] the coherence length $\xi(T,l_i) \simeq \xi_0(1+\xi_0/l_i)^{-1/2}$ which determines the diameter of the vortex core, pinning and vortex drag was confused with the decay length $\tilde{\xi} = (\xi_0^{-1} + l_i^{-1})^{-1}$ of the kernel $K(\mathbf{r}-\mathbf{r}')$ in the nonlocal relation, $\mathbf{J}(\mathbf{r}) = \int K(\mathbf{r}-\mathbf{r}')\mathbf{A}(\mathbf{r}')d^3\mathbf{r}'$ [10, 18]. As a result, the effect of the mean free path on R_i was calculated incorrectly
[295] Scanlan R M, Malozemoff A P and Larbalestier D C 2004 *Proc. IEEE* **92** 1639
[296] Haugan T J, Puig T, Matsumoto K and Wu J 2020 *Supercond. Sci. Technol.* **33** 040301
[297] Blatter G, Geshkenbein V B and Koopmann J A G 2004 *Phys. Rev. Lett.* **92** 067009
[298] Gurevich A 2014 *Annu. Rev. Condens. Matter Phys.* **5** 35
[299] Kwok W-K, Welp U, Glatz A, Koshelev A E, Kihlstrom K J and Crabtree G W 2016 *Rep. Prog. Phys.* **79** 116501
[300] Kirkpatrick S 1973 *Rev. Mod. Phys.* **45** 574
[301] Landauer R 1952 *J. Appl. Phys.* **23** 779
[302] Mkrtchyan G S and Shmidt V V 1972 *Sov. Phys.—JETP* **34** 195
[303] Buzdin A I and Feinberg D 1996 *Physica* C **256** 303
[304] Place A P M *et al* 2021 *Nat. Commun.* **12** 1779
[305] Wang C *et al* 2022 *npj Quantum Inf.* **8** 3